Tensor polarization in elastic electron-deuteron scattering in the momentum transfer range $3.8 \leq Q \leq 4.6$ fm^{-1}

M. Garçon,[5,6] J. Arvieux,[7] D. H. Beck,[2,3] E. J. Beise,[5] A. Boudard,[6] E. B. Cairns,[1] J. M. Cameron,[1,4] G. W. Dodson,[5] K. A. Dow,[5] M. Farkhondeh,[5] H. W. Fielding,[1] J. B. Flanz,[5] R. Goloskie,[9] S. Høibråten,[5] J. Jourdan,[2] S. Kowalski,[5] C. Lapointe,[1] W. J. McDonald,[1] B. Ni,[4] L. D. Pham,[5] R. P. Redwine,[5] N. L. Rodning,[1] G. Roy,[1] M. E. Schulze,[8] P. A. Souder,[8] J. Soukup,[1] I. The,[5] W. E. Turchinetz,[5] C. F. Williamson,[5] K. E. Wilson,[5] S. A. Wood,[3,5] and W. Ziegler[1]

[1] *University of Alberta, Edmonton, Alberta, Canada T6G 2N5*
[2] *California Institute of Technology, Pasadena, California 91125*
[3] *University of Illinois, Champaign, Illinois 61820*
[4] *Indiana University Cyclotron Facility, Bloomington, Indiana 47405*
[5] *Massachusetts Institute of Technology, Cambridge, Massachusetts 02139*
[6] *Service de Physique Nucléaire, Centre d'Etudes Nucléaires de Saclay, 91191 Gif-sur-Yvette, France*
[7] *Laboratoire National Saturne, 91191 Gif-sur-Yvette, France*
[8] *Syracuse University, Syracuse, New York 13210*
[9] *Worcester Polytechnic Institute, Worchester, Massachusetts 01609*

(Received 3 May 1993)

The tensor polarization of the recoil deuteron in elastic electron-deuteron scattering has been measured at the Bates Linear Accelerator Center at three values of four-momentum transfer, $Q =$ 3.78, 4.22, and 4.62 fm^{-1}, corresponding to incident electron energies of 653, 755, and 853 MeV. The scattered electrons and the recoil deuterons were detected in coincidence. The recoil deuterons were transported to a liquid hydrogen target to undergo a second scattering. The angular distribution of the $\vec{d}$-p scattering was measured using a polarimeter. The polarimeter was calibrated in an auxiliary experiment using a polarized deuteron beam at the Laboratoire National Saturne. A Monte Carlo procedure was used to generate interpolated calibration data because the energy spread in the deuteron energies in the Bates experiment spanned the range of deuteron energies in the calibration experiment. The extracted values of t_{20} are compared to predictions of different theoretical models of the electromagnetic form factors of the deuteron: nonrelativistic and relativistic nucleon-meson dynamics, Skyrme model, quark models, and perturbative quantum chromodynamics. Along with the world data on the structure functions $A(Q)$ and $B(Q)$, they are used to separate the charge monopole and charge quadrupole form factors of the deuteron. A node in the charge monopole form factor is observed at $Q = 4.39 \pm 0.16$ fm^{-1}.

PACS number(s): 25.30.Bf, 24.70.+s, 25.10.+s, 27.10.+h

I. INTRODUCTION

The elastic form factors for elastic scattering from deuterium (e-d) have been the subject of intensive experimental and theoretical studies for several decades. They contribute significantly to the determination of the basic nature of the nucleon-nucleon interaction (NN), especially its off-shell properties, its behavior at short distances, and the role of non-nucleonic degrees of freedom.

Since the deuteron has spin 1, its electromagnetic structure is described by three form factors: charge monopole G_C, charge quadrupole G_Q, and magnetic dipole G_M. Nonrelativistically, these form factors are related to the spatial distributions of charge, quadrupole deformation and magnetization, respectively. Both the nucleon spins and the nucleon current contribute to the latter.

Many models of the deuteron electromagnetic form factors have been proposed in the literature. In the impulse approximation (IA) for the description of e-d scattering, the electron interacts with each nucleon in the deuteron via a virtual photon and the electromagnetic form factors of the interacting nucleon are taken to be the same as those for a free nucleon. At large four-momentum transfers, various corrections to the IA model become important. These include isoscalar meson-exchange currents (MEC), isobar components (IC), relativistic effects, and perhaps quark degrees of freedom. Relativistic models have been developed both in the light cone formalism and by solving a Bethe-Salpeter equation. Some nonrelativistic models used a coupled-channel formalism of nucleons and isobars (Δ and N^*) and include contributions from MEC; in these models, the amount of Δ-Δ component in the deuteron can be quite small, about 0.4%, but also as high as 7%. Quark configurations are incorporated in several hybrid quark-hadron models with a quark confinement radius taken as a free parameter, usually about 0.5 fm. Some of these hybrid models give predictions similar to those of the IA model while others have completely different results for the high four-momentum transfer region. A Skyrme model, which is equivalent to a low energy version of QCD in the limit of a large number of colors, determines the form of the

one-body and two-body exchange current operators from the fields of the Lagrangian and predicts results for the deuteron form factors similar to those obtained from conventional nucleon-meson dynamics. Finally, perturbative quantum chromodynamics (PQCD) predicts simple relations between the form factors of the deuteron.

Experimentally, at least three observables from *e-d* scattering are needed to determine separately all three form factors. Most experiments to date have measured differential cross sections. Measurements at different electron angles for the same four-momentum transfer allow the determination of the longitudinal and transverse structure functions $A(G_C, G_Q, G_M)$ and $B(G_M)$, which so far have been the only testing ground for the above-mentioned models. A is measured up to $Q = 10$ fm^{-1} [1] and B up to $= 8$ fm^{-1} [2]. To separate further G_C and G_Q, the measurement of another observable is required, and this is necessarily a polarization observable. This was realized a long time ago: one must either measure the asymmetries induced by a tensor polarized deuterium target or measure the tensor polarization of the recoil deuterons (alternatively, one may deal with deuteron vector polarization only if the electron beam is polarized; this type of experiment has never been attempted). The observable of choice is the tensor moment t_{20} which is a measure of the relative probabilities of scattering off deuterons in magnetic substates $m_z = +1$, -1, or 0 when dealing with a polarized target, or of producing deuterons in these different magnetic substates when measuring the polarization of the outgoing deuterons. By convention, the spin quantization axis is chosen along the direction of the momentum transfer. $t_{20}(G_C, G_Q, G_M, \theta_e)$, together with $A(G_C, G_Q, G_M)$ and $B(G_M)$, allows the separate determination of the two charge form factors G_C and G_Q (θ_e is the electron scattering angle). The tensor moments t_{21} and t_{22} provide other useful quadratic combinations of the form factors.

Previous measurements of t_{20} [3–6] have been performed at relatively low momentum transfer where theoretical uncertainties are very small. We report here on measurements of all three moments of the recoil deuteron tensor polarization (t_{20}, t_{21}, and t_{22}) at four-momentum transfer values of 3.78, 4.22, and 4.62 fm^{-1}, at angles such that the magnetic contribution to t_{20} is small. In this four-momentum transfer range, G_C is expected in most models to pass through zero, this being a reflection of a node in the S-state wave function, which in turn is due to the repulsive nature of the NN interaction at short distances [7]; thus the already measured structure function A determines mostly G_Q. At such four-momentum transfers, short-range components and non-nucleonic contributions become important and manifest themselves mostly in G_C. Finally, contrary to all other observables and to the form factors themselves, t_{20} is nearly independent of the elementary nucleon form factors, and in particular of the poorly known neutron electric form factor.

A. Kinematics and observables

In the elastic scattering of an ultrarelativistic electron of energy E_e off a deuteron of mass M_d at a laboratory angle θ_e, the energy $E_{e'}$ of the electron in the final state is given by

$$E_{e'} = E_e/f \ , \tag{1}$$

where f is usually called the recoil factor:

$$f = 1 + \frac{2E_e}{M_d}\sin^2\frac{\theta_e}{2} \ . \tag{2}$$

We define Q, related to the spacelike four-momentum q transferred from the electron to the target nucleus, by

$$Q^2 \equiv -q^2 = 4\frac{E_e^2}{f}\sin^2\frac{\theta_e}{2} \ . \tag{3}$$

For completeness, the kinetic energy and the angle of the recoil deuteron are given below:

$$E_d = E_{e'} - E_e = \frac{Q^2}{2M_d} \ , \tag{4}$$

$$\sin^2\theta_d = \frac{\cos^2(\theta_e/2)}{f + (E_d/M_d)^2\sin^2(\theta_e/2)} \ . \tag{5}$$

The general features of *e-d* scattering have been investigated by many authors [8–11]. By using the first Born approximation (one-photon exchange approximation) and imposing relativistic and gauge invariance, the differential cross section can be written as

$$\frac{d\sigma}{d\Omega} = \left(\frac{d\sigma}{d\Omega}\right)_{\text{Mott}} S \ , \tag{6}$$

where

$$\left(\frac{d\sigma}{d\Omega}\right)_{\text{Mott}} = \frac{1}{f}\frac{\alpha^2\cos^2(\theta_e/2)}{4E_e^2\sin^4(\theta_e/2)} \tag{7}$$

describes the scattering of an electron off a pointlike spinless particle (α is the fine structure constant), and

$$S = A(Q) + B(Q)\tan^2\frac{\theta_e}{2} \tag{8}$$

originates from the electromagnetic structure of the deuteron. As a consequence of parity and time-reversal invariance, the structure functions A and B are in turn given in terms of three elementary electromagnetic form factors:

$$A(Q) = G_C^2(Q) + \frac{8}{9}\eta^2 G_Q^2(Q) + \frac{2}{3}\eta G_M^2(Q) \ , \tag{9}$$

$$B(Q) = \frac{4}{3}\eta(1+\eta)G_M^2(Q) \tag{10}$$

with $\eta = Q^2/4M_d^2$. The three moments t_{2q} of the deuteron tensor polarization are given by [12,13]

$$t_{20} = -\frac{1}{\sqrt{2}}S\left[\frac{8}{3}\eta G_C G_Q + \frac{8}{9}\eta^2 G_Q^2 + \frac{1}{3}\eta\left(1 + 2(1+\eta)\tan^2\frac{\theta_e}{2}\right)G_M^2\right] \ , \tag{11}$$

$$t_{21} = \frac{2}{\sqrt{3}\mathcal{S}}\eta\left(\eta + \eta^2 \sin^2\frac{\theta_e}{2}\right)^{1/2} G_M G_Q \sec\frac{\theta_e}{2} , \quad (12)$$

$$t_{22} = -\frac{1}{2\sqrt{3}\mathcal{S}}\eta G_M^2 . \quad (13)$$

In the one-photon exchange approximation of e-d scattering, and as a result of time-reversal invariance, the deuteron vector polarization is identically zero when using an unpolarized electron beam [14]. The form factors are normalized at $Q = 0$ to the static moments:

$$G_C(0) = 1 , \quad (14a)$$

$$G_Q(0) = M_d^2 \mathcal{Q}_d = 25.83 , \quad (14b)$$

$$G_M(0) = \frac{M_d}{M_p}\mu_d = 1.714 , \quad (14c)$$

where $\mathcal{Q}_d$ and μ_d are, respectively, the electric quadrupole moment and the magnetic dipole moment of the deuteron, and M_p is the proton mass.

The quantity $\tilde{t}_{20}$, derived from Eq. (11) by neglecting the magnetic contribution, is often used in the literature. Though not actually an observable, it is interesting because it depends solely on the ratio

$$x = \frac{2}{3}\eta G_Q / G_C , \quad (15)$$

$$\tilde{t}_{20} = -\sqrt{2}\frac{x(x+2)}{1+2x^2} . \quad (16)$$

At small four-momentum transfers, $x \ll 1$ and $t_{20} \simeq \tilde{t}_{20} \simeq -2x\sqrt{2} \simeq -(\sqrt{2}/3)\mathcal{Q}_d Q^2$, so that t_{20} is very much constrained by the already known deuteron quadrupole moment ($\mathcal{Q}_d = 0.2859$ fm^2). In fact this approximation works very well up to 2.5 fm^{-1}, meaning that G_C and G_Q have similar Q dependence up to this momentum transfer. In the Q range where $\tilde{t}_{20}$ is expected to reach its absolute minimum $-\sqrt{2}$ ($x = 1$), the approximation $t_{20} \simeq \tilde{t}_{20}$ is only valid to 10–15% for $\theta_e \simeq 70°$.

B. This experiment

The goal of this experiment was to extend to the highest possible Q values the measurements of t_{20} and to measure simultaneously all three tensor moments. Elastic e-d events were identified by a coincidence between the scattered electrons and the recoil deuterons. The polarization of the recoil deuterons was measured in a polarimeter. In the range of four-momentum transfer where the charge monopole form factor is expected to pass through zero ($Q \simeq 4$ fm^{-1}), the recoil deuterons have a kinetic energy of about 170 MeV according to Eq. (4). Prior to this experiment, a search was made for efficient reactions with sizeable analyzing powers in this energy range [15]. Deuteron-proton (d-p) scattering was found to be the best candidate. A polarimeter [16] based on this reaction was built and calibrated using a deuteron beam of known polarization at the Laboratoire National Saturne (France). This polarimeter was then installed at the end of a specially designed deuteron transport channel at the MIT–Bates Linear Accelerator Center. The tensor moments t_{kq} of the recoil deuteron polarization induce a modification of the shape of the angular distribution of d-p events as compared to the scattering of unpolarized deuterons. This characteristic change of shape was used quantitatively to determine the tensor polarization of the recoil deuterons in e-d scattering.

In this double scattering experiment, owing to the smallness of the e-d cross sections, a thick liquid deuterium target, large solid angles for the electron and deuteron spectrometers, and a high efficiency for the deuteron polarimeter were needed to obtain a sufficient number of events. All these, as well as other equipment, will be described in the next section. The data analysis and the results are discussed in Sec. III. Special care was taken to understand, with the help of a Monte Carlo simulation, any possible differences in the polarimeter response between the calibration at Saturne and this experiment at Bates. In Sec. IV the individual charge form factors G_C and G_Q will be extracted using the polarization observables as well as existing data on the structure functions A and B. Our results will finally be compared with theory in Sec. V.

A shorter account of our t_{20} results was previously published in a Letter [17]. This paper (see also [18]) describes the details of the experiment and of its analysis, presents the data for t_{21} and t_{22}, and explores further the physical significance of our results. Its organization deliberately follows the publication of the latest measurements of $B(Q)$ [2]: the same theoretical calculations may then be easily compared against different observables and the reader should benefit from this complementarity.

II. EXPERIMENTAL APPARATUS

The experiment was performed on beam line B of the South Experimental Hall at the MIT-Bates Linear Accelerator Center. The experimental arrangement is sketched in Fig. 1.

This measurement of the deuteron tensor polarization was a coincident, double scattering experiment. Unpolarized electrons were incident upon an unpolarized liquid deuterium (LD_2) target. The elastically scattered electrons were detected in the magnetic spectrometer OHIPS. The deuterons were detected at a fixed angle of 41° while at each beam energy the electron spectrometer was moved to the kinematically correlated scattering angle. It was necessary to detect the scattered electrons and the recoil deuterons in coincidence to identify e-d events because of the large background due to protons coming from photodisintegration of the deuterons in the target. The recoil deuterons, having possible tensor moments of the polarization t_{20}, t_{21}, and t_{22}, were transported using a magnetic transport channel to a liquid hydrogen (LH_2) target where a fraction of them underwent a second scattering. The channel, along with a carbon de-

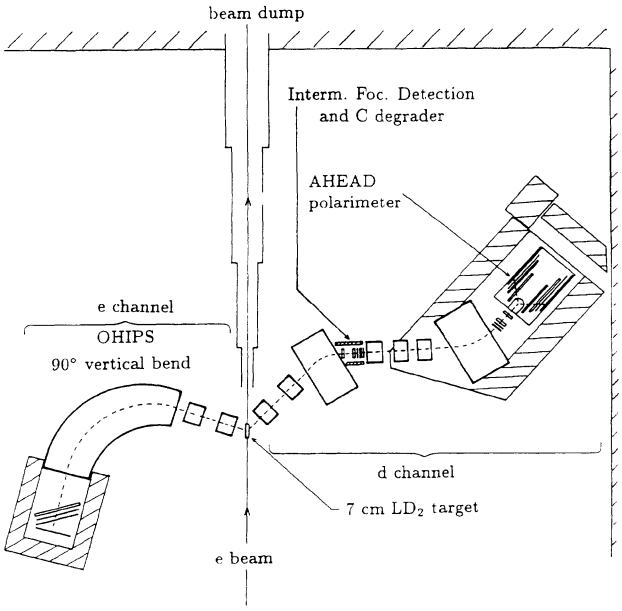

FIG. 1. Layout of the experimental setup.

grader, was designed partially to separate the protons from the deuterons. After the second scattering, the angular distribution of the $\vec{d}$-p scattering was measured in a polarimeter.

A. Electron beam

The Bates recirculated electron linear accelerator [19] delivered a pulsed beam with a pulse length of 13 μs at a repetition rate of 600 Hz. The average current was 5 to 30 μA, as measured by two nonintercepting toroids [20].

Each of our three data points was taken at a different beam energy. This energy was first determined by a special reference dipole on a separate beam line during the tuning of the beam while its final and more precise value was obtained after the experiment through the analysis of the elastic electron peak in OHIPS (see Sec. III A). The energy spread of the beam was kept lower than 0.3% by the use of appropriate defining slits along the beam path.

Several sensors monitored the beam position and spot size just upstream of the LD_2 target. A scintillating BeO target and a secondary emission monitor made of an aluminium foil having a rectangular aperture of 9 mm (horizontal)×7 mm (vertical) were used to prevent misalignment of the beam with respect to the target position. an insulated grid of two horizontal foils separated by 3 mm and two vertical wires separated by 5 mm defined the minimum beam spot size that could be delivered to prevent excessive current density in the target cell. A missing signal in one or more wires or excessive current on the secondary emission monitor would sound an alarm and could be used to disable the electron gun at the accelerator source. In addition, signals induced in a cavity of the traveling wave type gave redundant information on the beam position and were displayed in the counting room. The beam spot size at the target was adjusted to about 7 mm (horizontal)×5 mm (vertical).

Downstream of the target, the beam traveled through a widening vacuum pipe to an encaved beam dump. Special care was taken to shield heavily the detectors from this beam pipe and from the beam dump.

B. Liquid deuterium target

Based on a previously used design [21], a closed loop system containing 9.5 liters of circulating liquid deuterium was used as the primary target in the experiment. The target loop was constructed of stainless steel except for the target section which was built from aluminium. The wall thickness at the target section at beam level was 0.63 mm. The target length along the beam was 7 cm, and its width 2 cm. Along the direction of the scattered electrons and deuterons, the target was collimated to a useful length of 5 cm with tungsten blocks to remove background events originating from the entrance and exit parts of the target wall.

A 200 W refrigeration system consisting of a two-stage compressor and a Koch model 1420 cryogenic expansion refrigerator provided cold gaseous helium to a counterflow heat exchanger in the target loop, in order to cool and to maintain the liquid at low temperature. Two vane-axial fans circulated the liquid through the loop at a speed of about 2 m/s. At this speed and at a beam repetition rate of 600 Hz, a given parcel of liquid would move by about 4.8 mm between successive beam pulses. Therefore, at most only two beam pulses would be incident on a given parcel of liquid; this parcel would be quickly dispersed through the bulk liquid due to the highly turbulent flow (Reynolds number approximately 200 000). Two heaters provided a constant or variable heat load to adjust the operating conditions. The loop was equipped with various temperature and pressure sensors and a liquid level sensor.

An 8085-microprocessor based system was used to control and monitor the operation of the target. Information from the temperature sensors and pressure transducers was transferred to a μVAX for recording on tape and display as a function of time for long-term monitoring. The measured value of the beam current was used to adjust automatically, with the heaters, the total thermal load to a preset value.

The target was operated at around 20 K for a total heat load of 100 W. An average beam current of 20 μA deposited about 60 W in the target. The operating pressure was 1 to 2 atm. Under these conditions, there was no evidence for local boiling along the beam path up to 30 μA of beam average intensity, as monitored by the electron counting rates.

More details about the deuterium handling and control systems can be found in [18,22].

C. Electron spectrometer

The scattered electrons were detected in the One Hundred Inch Proton Spectrometer (OHIPS), which consists

of a quadrupole doublet and a dipole. Each quadrupole has an aperture radius of 30.5 cm and a physical length of 61 cm. The dipole, which bends electrons by 90° in the vertical direction, has an arc radius of 2.54 m. The magnetic field of the dipole was measured using a Rawson probe. The magnets along with the shielded detectors are assembled into a single structure mounted on air pads. The drift distance between the target and the first quadrupole was adjusted to give the maximal solid angle of 18 msr (±30 mrad in the horizontal plane, ±155 mrad in the vertical plane). The quadrupole magnets were successively focusing and defocusing in the vertical dispersive plane. The optics provided point-to-point focusing in both planes.

The OHIPS detection system consisted of a VDCX (vertical drift chamber crossed [23]) and two scintillators S0 and S1 (71.1 cm×20.3 cm×0.5 cm), all tilted along the focal plane direction. A third scintillator S2 (63.5 cm×17.8 cm×3.8 cm) was placed in a horizontal position. The VDCX had two planes of orthogonal active wires. After amplification and discrimination, the signals from the wires were fed into a delay line. The measurement of the time elapsed between these signals and the coincidence of the scintillators allowed the particle positions and angles to be reconstructed from the drift time in the chamber.

The scintillators S0 and S1 were used in the main trigger and provided time of flight (TOF) information between both arms. The VDCX information was used only for tuning and to determine the beam energy (see Sec. III A).

D. Deuteron transport channel

A magnetic transport channel was specially designed to transport recoil deuterons from the LD_2 target to the polarimeter and to match the acceptance of OHIPS for elastic electrons, thereby maximizing the flux of tagged deuterons entering the polarimeter target. The channel consisted of a QQD-QQQD system (Fig. 1), where Q stands for a quadrupole and D for a dipole. It was set at a fixed deuteron production angle of 41°. An intermediate focus detection system (IFD) and, for our points at $Q = 4.22$ and 4.62 fm^{-1}, a carbon energy degrader (CED) were placed between the first dipole and the third quadrupole. Background protons with the same initial momentum as the recoil deuterons from *e-d* scattering lost a smaller amount of momentum in the CED, therefore were bent less in the second dipole, and most did not enter the polarimeter LH_2 target. The channel thus operated as a partial isotope separator. The energy degradation was also necessary because of the field limitation in the second dipole and to a lesser extent to have the deuteron energy fall within the energy range of maximum efficiency for the polarimeter.

Both dipole magnets bent the deuterons by an angle $\theta_B = 35°$ but in opposite directions so that the bend in the second dipole cancelled most of the spin precession effect due to the bend in the first dipole. The residual spin precession due to the energy loss of the deuterons passing through various materials between the two dipoles (mostly IFD and CED), $\lambda = (\gamma_{D_1} - \gamma_{D_2})(\mu_d - 1)\theta_B$ (γ_{D_i} is the usual relativistic γ factor corresponding to the deuteron energy in each dipole), was at most 3 mrad. Since the effect on the observables t_{kq} is of order λ^2, it was neglected.

The first three quadrupoles had an aperture diameter of 20.3 cm and a physical length of 61 cm. The last two quadrupoles and the second dipole were part of an existing spectrometer at Bates, assembled as a single structure named Bigbite [24]. The Bigbite quadrupoles had an aperture diameter of 20.3 cm and a physical length of 38.1 cm. The Bigbite dipole had a gap of 25.4 cm and a physical length of 101.6 cm. The first dipole had a gap of 15.2 cm and a physical length of 91.4 cm. The field maps of all these magnets were measured for a proper channel design and the field probes of the dipoles were calibrated prior to the experiment. A vacuum chamber with windows made of kapton was installed in the QQD system. Because of an accident, it was replaced for our last two data points by a plastic bag filled with helium gas. Such a bag was placed as well in the second half of the deuteron channel (QQQD).

The QQD and QQQD systems were each designed to have point-to-point focusing using the computer code TRANSPORT [25]. A more detailed study of the transmission of deuteron flux in the channel was done using the Monte Carlo code REVMOC [26] which took into account not only the optics of the channel up to second order, but also the effects of magnet apertures, energy losses and straggling, multiple scattering, nuclear elastic scattering and nuclear absorption. All materials from the LD_2 target up to the entrance of the LH_2 target in the polarimeter were included in the simulation.

A distribution of recoil deuterons originating from *e-d* scattering at the LD_2 target was generated using a Monte Carlo code. In generating the deuteron distribution, the code took into account the target length, the shape of the electron beam profile, the incident electron beam energy and its spread, the energy loss of the electrons in LD_2 and the differential elastic cross section for *e-d* scattering. The deuteron distribution generated by this code was then used as input for REVMOC. REVMOC was used to optimize the ratio $\mathcal{R}$ of the number of deuterons entering the polarimeter LH_2 target to the number of deuterons coming from *e-d* scattering by varying the field strengths of the quadrupoles or the drift distances between the magnetic elements. The ratio $\mathcal{R}$ was thus predicted to be about 27% and relatively independent of the deuteron energies at our three Q values. Deuterons were lost in the channel due to its finite transverse dimensions (24% of unavoidable mismatch with the electron spectrometer, 24% in the transmission), multiple scattering (8–14%), nuclear absorption (10–20%), and elastic nuclear scattering (2.5%). Experimentally, the ratio $\mathcal{R}$ was found to range from 23 to 34% by comparing the measured *e-d* event rate to the calculated rate from the known cross section and from the OHIPS solid angle.

E. Intermediate focus detection

The IFD was placed after the QQD magnetic focus point. It consisted successively of two multiwire proportional chambers (MWPC's), a hodoscopoe of ten small scintillators and an intermediate focus large scintillator (IFS). A lead collimator was placed between the two MWPC's in order to cut some of the proton flux downstream, while the carbon energy degrader (CED) was placed between the hodoscope and IFS.

Each MWPC had two active planes of 96 active wires each, with a 2 mm spacing, read out using a LeCroy PCOS III system. The MWPC's were used to tune the first half of the deuteron channel at the beginning of each run. During the run, they were used only to monitor this tune, but the particle trajectory at the IFD was not reconstructed in the data analysis because of a high hit multiplicity on the wires. The instantaneous count rates on the whole IFD were up to 1 MHz per μA of the average beam intensity.

The IFS (15.24 cm×15.24 cm×0.32 cm) was used only during the run taken at the lowest luminosity (the lowest Q point), in coincidence with signals from the hodoscope.

Each hodoscope scintillator had dimensions of 1.25 cm×10 cm×0.3 cm. A 2.54 cm Hamamatsu R1450 photomultiplier was connected to each scintillator through a fiber optics light guide. The hodoscope was used to provide a trigger to the MWPC's and to identify deuterons by pulse height information and by time of flight (TOF) measurements between OHIPS and the IFD and between the IFD and the polarimeter.

F. Polarimeter

As mentioned previously, a second scattering was required to measure the polarization of the deuterons. The polarized deuterons coming from e-d scattering were transported through the deuteron transport channel to the Alberta High Efficiency Analyzer for Deuterons (AHEAD) polarimeter. The AHEAD polarimeter (Fig. 2) consisted of two front end (FE) MWPC's to reconstruct incident tracks, an LH_2 target to provide the second scattering, two cylindical wire chambers (CWC's) to reconstruct tracks of outgoing particles (a proton and/or a deuteron), and segmented ΔE-E scintillators to identify detected particles. The polarimeter was capable of measuring both the vector (zero in the case of e-d scattering) and tensor components of the polarization. It was designed to cover a complete angular range of 360° in azimuthal angles φ and of 17° to 90° in polar scattering angles, corresponding to the angular range 30° to 160° in the d-p elastic scattering center of mass angle θ. The design, construction and calibration of the AHEAD polarimeter have been described in a previous paper [16]. Only the major components will be described here, with special attention to details relevant for this experiment.

Incident deuterons entering the polarimeter first passed through two thin FE plastic scintillators (15.2 cm×15.2 cm×0.3 cm) which provided a trigger to the two FE multiwire proportional chambers. Each chamber had x and y planes of 192 wires with 1 mm spacing and 96 wires with 2 mm spacing, respectively. A LeCroy PCOS III system was used to read out the MWPC's.

The LH_2 target had a diameter of 10 cm and a length of 27 cm. It protruded horizontally into the detector assembly for proper scattering angle coverage. In order to minimize energy losses of the scattered particles, the LH_2 target wall was constructed from 0.25 mm mylar and the surrounding vacuum jacket was made of a 1-mm-thick spun aluminum domed snout.

The trajectories of the scattered particles, deuterons and protons, exiting the LH_2 target were measured by two cylindrical wire chambers (CWC's). The inner and outer CWC's had radii of 8.62 cm and 17.62 cm and lengths of 68.5 cm and 92.0 cm, respectively. The CWC's walls were also designed to minimize energy loss of the scattered particles and were built of polyurethane foam

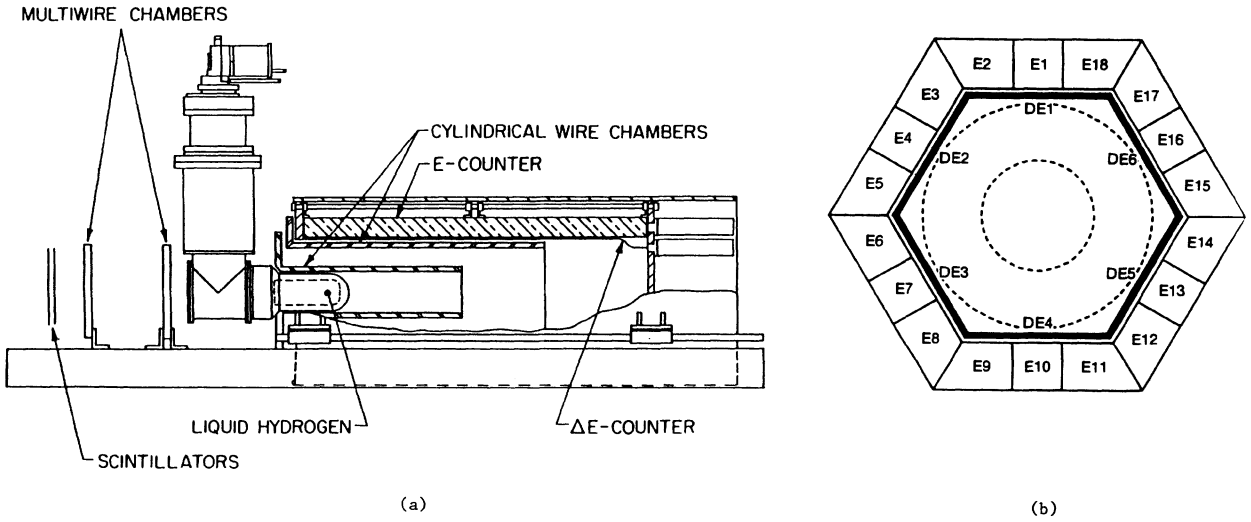

FIG. 2. Schematic view of the AHEAD polarimeter, (a) along the incident deuteron direction, (b) in the transverse plane.

cylinders pressed between graphite coated kapton foils. The stainless steel anode wires were strung longitudinally along the cylinder in a U shape, with signal amplifiers mounted at the upstream end of the CWC's. A pulser input was installed at the center of each wire at the downstream end of the CWC's for amplifier calibration and testing. The particle position along the wire was measured using a charge division method. With the CWC's operating in the limited streamer mode, a resolution of about 1 cm (FWHM) was achieved at the wire center, deteriorating to about 4 cm at the end. Each half wire was placed in a cell (0.9 cm×0.9 cm) which was separated from the neighboring cell using kapton ribbon, sprayed with graphite, and strung longitudinally between the two cylindrical polyurethane walls. The chambers were filled with a gas mixture of 20% argon and 80% isobutane and operated at a negative high voltage of 3200 V on the cathode walls. Lecroy FASTBUS ADC's were used to digitize the output charge from custom amplifiers [16] and the data were transferred to a CES 2180 STARBURST fast processor.

The CWC assembly was surrounded by two concentric layers of segmented plastic scintillators 1.5 m in length. The first layer consisted of thin scintillators (3 mm thick) to provide a ΔE signal and the second layer of thick (7.6 cm) NE110 plastic scintillators (E) to absorb the remaining energy of the scattered particles that passed the ΔE scintillators. The ΔE array was divided into 6 scintillators while the E array had 18. Each scintillator was read at its downstream end by a photomultiplier. The attenuation of the light signal in the scintillator material was measured using radioactive sources and the measured attenuation factor was used to correct the measured signals in the data analysis. The raw analog signals were digitized using CAMAC ADC's and the stability of the photomultipliers was monitored using a light pulse generated by LED's. The ΔE and E scintillators also provided TOF information from the FE scintillators. The CAMAC ADC and TDC modules were read by the STARBURST processor.

During the run taken at the lowest Q value, an excess of background protons was observed in the polarimeter detectors in the horizontal plane. To prevent pileup and false asymmetry measurement, tungsten blocks were inserted in front of the polarimeter for runs at the two highest Q values where the two hot spots had been observed. For this purpose, the whole assembly of the CWC's and the ΔE-E scintillators had to be moved downstream by 6.1 cm with respect to the LH_2 target.

G. Trigger electronics and data acquisition

The trigger electronics logic was organized to sort and label four types of events, ordered in the following hierarchy of priority: (i) Pulser events monitored the stability of the CWC's and the ΔE-E scintillators. (ii) A coincidence from OHIPS, IFD, the first FE scintillator and any of the 6 ΔE counters defined a polarimeter event (POL). (iii) A coincidence from OHIPS, IFD, and the first FE scintillator defined front end (FE) events because they caused the FE scintillators to fire but did not trigger any of the ΔE counters, meaning that there was no scattering in the LH_2 target. These events were prescaled. (iv) A prescaled number of OHIPS singles events were used for tuning purposes.

During test runs, the elastic e-d events were easily identified in TOF distributions, one between OHIPS and FE, the other one between IFD and FE. The background protons were uniformly distributed in the first variable, since they did not correspond to real coincidences between the two arms, but appeared as a clearly separated peak in the IFD-FE TOF spectrum. During data taking the protons were removed at the trigger level by a tight time coincidence between IFD and FE.

A μVAX II workstation was used, in conjunction with the acquisition program "Q" [27], to acquire and store data from events and from various scalers onto magnetic tape. It also processed and displayed some of the data on-line.

III. DATA ANALYSIS AND RESULTS

A. Electron-deuteron scattering

The elastic e-d events were easily selected by redundant cuts in TOF OHIPS-FE distributions and in pulse height spectra in FE and IFD hodoscope scintillators (Fig. 3). An empty target measurement showed no significant contribution of deuterons to the same spectra.

The only physical process which could imitate an e-d scattering is $\gamma d \rightarrow \pi^0 d$: the photon would originate from the very end of the Bremsstrahlung spectrum emitted by the beam as it traverses the target, and the π^0 could result, via its 2γ decay and subsequent photon conversion,

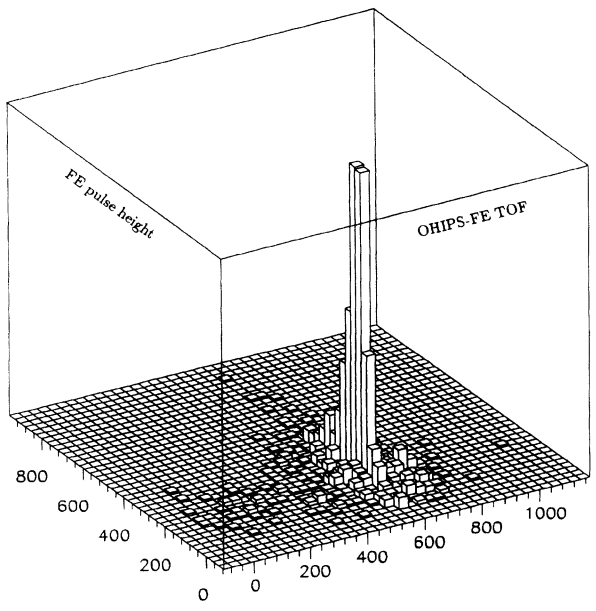

FIG. 3. FE pulse height vs OHIPS-FE-TOF (arbitrary units). The peak corresponds to e-d events.

TABLE I. Experimental and analysis conditions. The average energies incident on the polarimeter (both for the experiment and for the calibration) are followed by the range of corresponding vertex energies. $\Delta E_d^{\rm inc}$ is the spread in deuteron incident energy for the Bates data.

Q (fm^{-1})	3.78	4.22	4.62
$\Delta Q_{\rm syst}$ (fm^{-1})	±0.02	±0.04	±0.02
CED thickness (cm)	0	1.13	4.0
$E_d^{\rm pol}$ (MeV)	133(61–120)		160(106–150)
$\Delta E_d^{\rm inc}$ (MeV)	14.3	16.5	23.0
Calibration data	120(81–110)		145(111–135)
	145(91–130)		170(126–150)
Particle identification	ΔE-E or ΔE-FE TOF		ΔE-E(E signal required)
Chamber cut	not applied		applied
$E_{\rm diff}$ cut	angle independent		angle dependent

in the detection of a correlated high energy electron in OHIPS. This contribution is kinematically at the very limit of our acceptance and was estimated to be negligible.

The position of the electron peak in OHIPS from e-d events was used to give a determination of the beam energy [using Eq. (1) with corrections for the electron energy losses in the target]. Another determination of E_e was provided by previous calibrations of the nominal beam energy and, for our highest Q point, by a special calibration run: the same beam was steered onto another beam line where high resolution measurements of elastic scattering off various thin solid targets were performed [28]. The OHIPS analysis of e-d events yielded beam energies slightly but systematically higher than the second method. E_e was arbitrarily chosen as the average between the two values, while their difference gave a measure of the systematic error of this determination. Using kinematics, Q and θ_e were determined from E_e and the precisely known deuteron channel angle θ_d. Systematic errors on Q estimated in this way appear in Table I.

The mean energy of deuterons at the entrance of the polarimeter ($E_d^{\rm pol}$) was measured by the field probe of the Bigbite dipole. It was confirmed by calculations of energy losses in the deuteron channel.

B. Deuteron-proton scattering

The yield for the scattering of tensor polarized deuterons in the AHEAD polarimeter is given by

$$N(\theta,\varphi) = kN_0(\theta,\varphi)[1 + t_{20}T_{20}(\theta) + 2t_{21}T_{21}(\theta)\cos\varphi + 2t_{22}T_{22}(\theta)\cos 2\varphi] , \quad (17)$$

where N_0 is the yield for scattering of unpolarized deuterons. In theory [29], N_0 is independent of φ; in practice, a φ dependence will appear owing to experimental asymmetries such as misalignment of the deuteron beam with respect to the polarimeter axis and nonuniform distribution of deuterons. The analyzing powers T_{kq} of the $\vec{d}$-p scattering were measured in the Saturne calibration experiment [16] while the goal of this experiment was to extract the tensor moments t_{kq} for deuterons coming from e-d scattering. k is an irrelevant normalization factor. Equation (17) is valid provided the same selection of d-p events has been performed for the Bates and Saturne experiments, i.e., the same incident deuteron positions, angles and energies, and also the same cuts for the analysis of the polarimeter events. Since this was not the case, N_0 was extracted from the calibration data, but properly weighted by the distribution of incident deuterons at the Bates experiment. This quantity will be referred to as the interpolated calibration data.

Differences between the two experiments had to be dealt with in the data analysis: (i) the average deuteron energies at Bates (133 MeV for the lowest Q point, 160 for the two other points) did not match any of the relevant calibration energies at Saturne (120, 145, 170 MeV). (ii) The incident deuteron energy spread was much larger at Bates than at Saturne; in addition to folding the polarimeter response over some energy range, this had the consequence of smearing polarimeter data on which cuts were applied for d-p selection (see the $E_{\rm diff}$ quantity below). (iii) For the two highest Q points at Bates, the polarimeter cylindrical detectors were shifted with respect to the LH_2 target (see Sec. II F), resulting in a different acceptance. (iv) At Saturne, the FE chambers were delay-line chambers, subsequently changed at Bates to handle the counting rates; the Bates FE analysis had to process the 15–20 % multiple hits events.

To account fully for the effect of the first three differences and to generate the proper interpolated calibration data, a Monte Carlo code was written. The Saturne calibration and the Bates experiment data were analyzed simultaneously.

1. Polarimeter event selection

First the position as given by the CWC's was calibrated: pulser data were used to adjust, when needed as a function of time, the relative gains of the two amplifiers at each wire end; proton-proton elastic scattering data taken in a special run at Bates determined the relative position of the two circular chambers by measuring the opening angle between the two scattered protons; the absolute positioning of the CWC's with respect to the LH_2

target was determined using data taken with a collimated radioactive source.

After a low cut on the total charge collected on each wire, all possible tracks resulting from the association of two hits in the inner and outer CWC's were considered. Tracks not originating from the target volume were rejected. Only events with one or two good tracks were selected. The intersection between the scattered particle(s) and incident deuteron trajectories defined the vertex coordinates. In case of multiple hits in the FE MWPC's the solution which gave the smallest distance between these trajectories was selected. Whenever this distance exceeded 3 cm, events were rejected.

The energy scales of the ΔE and E counters were then adjusted. This was an iterative procedure because energies were calculated for a given type of particle (protons or deuterons) and particle identification required the energy calibration. For each ΔE and E counter, a quantity $E_{\rm diff}$ was defined as the difference between the expected energy deposition and the measured value. The measured value was corrected for position dependent light attenuation in the scintillator and multiplied by an adjustable scale factor; the expected value was calculated using the nature of the particle, the scattering angle, *d-p* elastic scattering kinematics at the average incident energy $E(E_d^{\rm pol}, Z)$ corresponding to the actual vertex position, and energy losses in all material from the vertex to the counter. The scale factors were adjusted to align all counters at $E_{\rm diff}$ =0. For the Saturne calibration, scattered protons were used in this procedure, since elastically scattered deuterons had too small energies to be detected at the lowest calibration energy $E_d = 120$ MeV. For the Bates data, the resolution on $E_{\rm diff}$ was affected by the incident energy spread and a proton $E_{\rm diff}$ peak was no longer clearly identified (Fig. 4); the energy scale factors were then adjusted using the $E_{\rm diff}$ spectra for deuterons. A small, but measured, correction was made to account for different amount of light generated by protons and deuterons in scintillators for the same energy loss. The width of the Bates $E_{\rm diff}$ spectra, when compared to the corresponding Saturne spectra, determined the incident deuterons' energy spread at Bates (see Table I).

The separation between protons and deuterons was obtained using differential energy loss versus total energy deposited and total energy deposited versus FE-ΔE TOF [Fig. 5(a)] correlations for the lowest Q point. For the two highest Q points, only the first of these two correlations [Fig. 5(b)] was used since the TOF was not available from the calibration data. For the remainder of the analysis, only polarimeter events with one recoil proton were considered, since these largely dominate over deuteron or deuteron-proton events in the useful kinematical range $100° < \theta < 160°$ where the analyzing power T_{20} is the largest [16] (see also Fig. 6).

A cut on the $E_{\rm diff}$ distributions was applied to keep only elastic and slightly inelastic protons, since highly inelastic (break-up) events exhibit smaller analyzing powers. Before applying this cut to the Saturne data, the corresponding spectra were randomized using a Gaussian distribution to take into account the effect of the energy spread of the incident deuterons at Bates. The $E_{\rm diff}$ cuts

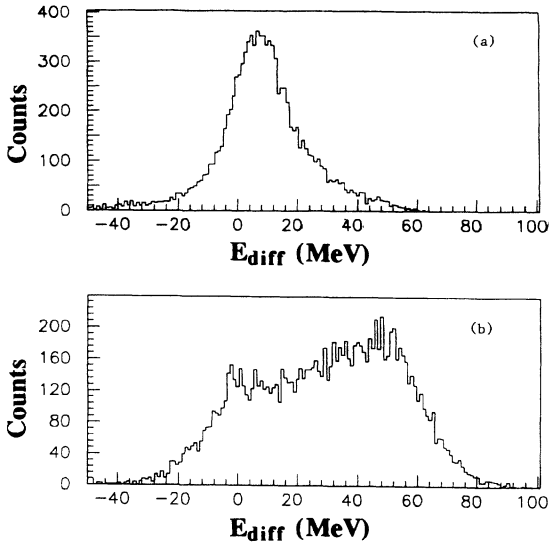

FIG. 4. $E_{\rm diff}$ distributions for all E scintillators, from the $E_d^{\rm pol} = 160$ MeV Bates data, for (a) scattered deuterons, (b) scattered protons. See text for definitions.

were chosen to be ±15 MeV for the Bates 133 MeV data and the Saturne 120 and 145 MeV data. For the Bates 160 MeV data and the corresponding Saturne 145 and 170 MeV data, an angle dependent cut was more appropriate since the $E_{\rm diff}$ resolution depended on angles: protons with $E_{\rm diff} > 10$ to 40 MeV depending on their angle were rejected.

As mentioned earlier, the cylindrical detection assembly was shifted downstream by 6.1 cm to accommodate shielding during the Bates experiment at $E_d^{\rm pol} = 160$

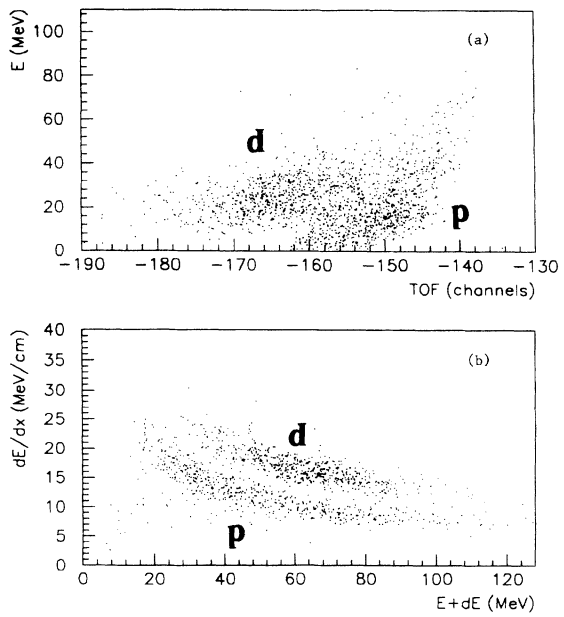

FIG. 5. Particle identification in AHEAD: (a) E-FE-ΔE TOF correlation for the run at $Q = 3.78$ fm^{-1}. (b) ΔE-E correlation for the run at $Q = 4.22$ fm^{-1}.

MeV (Q=4.22 and 4.62 fm^{-1}). To ensure equal acceptance in both cases, cuts were applied at the upstream end of the CWC's position spectra for the Saturne data and at their downstream end for the Bates data. Because of the finite position resolution of the chambers, these cuts were randomized; i.e., for each event a random cut normally distributed around the nominal value was applied.

Table I summarizes the analysis conditions.

The deuteron center-of-mass angle θ was calculated from the angle between the incident and recoil trajectories assuming elastic d-p scattering. The d-p events were then characterized by the incident deuteron average energy $E_d^{\rm pol}$, the vertex position $(\rho, \psi, Z$ in cylindrical coordinates), the scattering angles (θ, φ) and the $E_{\rm diff}$ value which for protons is a measure of the inelasticity of the reaction. The sensitivity of the polarimeter response to the incident deuterons' angle with respect to the polarimeter axis was found negligible and this information was not used subsequently. Because of the relatively small number of events, the Bates data could not be binned on all above variables and compared bin by bin to the Saturne calibration data. For each Bates point, only the variables θ and φ could be kept in the final analysis of Sec. III B 3. A proper account of folding over unwanted variables is described below. Formal considerations about this procedure are given in the Appendix.

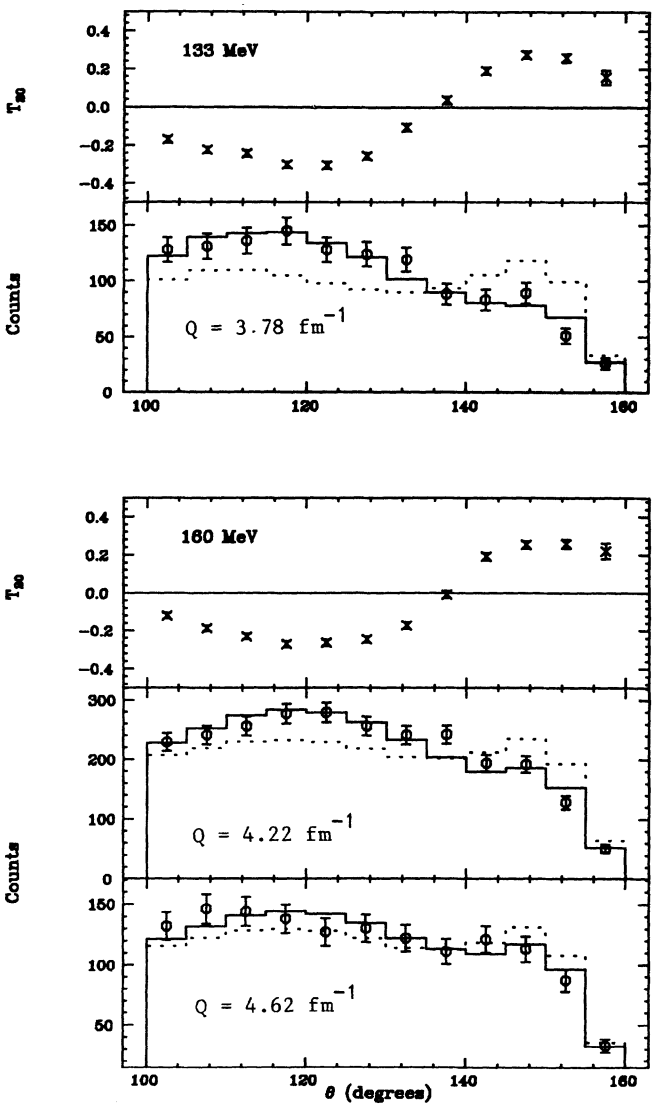

FIG. 6. Center-of-mass deuteron angle distributions for the analyzing power T_{20}, the Bates polarimeter data (open circles), the normalized interpolated calibration data ($k\mathcal{N}_0$, dotted histogram), and the fitted distribution ($\mathcal{N}$, solid histogram). See Eq. (19) for notations.

2. *Monte Carlo procedure*

A Monte Carlo routine [16,18] was used to calculate the effect of geometry, multiple scattering, wire chamber resolution, and absorption. Effective, unnormalized, angular distributions of the differential cross sections $\sigma_E(\theta)$ were extracted in an iterative procedure as the ratio of the Saturne data to the simulated acceptance. Due to the incident deuteron energy loss in the LH_2 target, the vertex energy $E(E_d^{\rm pol}, Z)$ varied in a wide enough range to allow for consistency checks for calibration runs at different energies E_d (see Fig. 11 in [16]) and to determine the effective cross sections to be used for the Bates energies. These in turn had to be weighted with the proper energy distribution to generate interpolated calibration data for the whole 27-cm-long target corresponding to the Bates incident energy $E_d^{\rm pol}$. The energy weighted factors $\mathcal{W}(E)$ were obtained in 5 MeV bins in the same way as the effective cross sections $\sigma_E(\theta)$. As the deuterons travel down the target, their absorption is compensated by the effect of increasing cross section with decreasing energy, so that the $\mathcal{W}(E)$ factors turned out to be nearly constant for the Saturne data at 145 and 170 MeV, as well as for the Bates data at 133 and 160 MeV. Consequently, and for convenience, the $\mathcal{W}(E)$ factors were taken from the Bates data instead of from the calibration data. The error due to this procedure is negligible. After extracting the effective cross sections and the energy weighting factors, interpolated calibration data $N_0(\theta, \varphi)$ at 133 and 160 MeV were generated using the Monte Carlo code. The spatial distributions of the incident deuteron beam were taken from a parametrization of the Bates FE events data. Gaussian distributions were used to represent the spread of the deuteron incident energy. On the basis of the REVMOC calculations, no correlation between position and energy of the incident deuterons was introduced.

3. *Extraction of tensor moments*

The yield of the scattering of tensor polarized deuterons measured in this experiment, $N_{\rm exp}$, was fitted using Eq. (17) with k and t_{kq} as free parameters. Due to the large angular dependence of the analyzing power $T_{20}(\theta)$, this method avoids the necessity of measuring the normalization factor k. Had T_{20} been a constant (as for

TABLE II. Experimental results for the three tensor moments and their statistical errors, with associated χ_t^2 per degree of freedom.

Q (fm^{-1})	θ_e (deg)	t_{20}	t_{21}	t_{22}	$\chi_t^2/139$
3.78	80.9	-1.24 ± 0.14	0.11 ± 0.18	0.48 ± 0.14	1.26
4.22	78.7	-0.82 ± 0.10	0.42 ± 0.12	-0.05 ± 0.09	1.74
4.62	76.7	-0.41 ± 0.13	0.57 ± 0.15	-0.04 ± 0.12	1.18

example in a previous t_{20} measurement [3]), then t_{20} and k would have been completely correlated and the absolute normalization would have had to be determined in both the experiment and the calibration.

The analyzing powers are nearly independent of energy [16] and were readily interpolated from the calibration energies. The yields for the Bates data and the interpolated calibration data covered the angular ranges $100° < \theta < 160°$ and $0° < \varphi < 360°$, each divided into 12 bins. Since some of the bins in the Bates data contained very few counts, Poisson statistics had to be used and the best estimates of the four parameters k and t_{kq} were obtained by minimizing the quantity [30]

$$\chi_t^2 = 2\sum_{j=1}^{144}\left[N(j) - N_{\rm exp}(j) + N_{\rm exp}(j)\ln\frac{N_{\rm exp}(j)}{N(j)}\right] , \tag{18}$$

where $N(j)$ is given by Eq. (17). χ_t^2 is expected to follow a χ^2 distribution with 139 degrees of freedom. The minimization was carried out numerically using the code MINUIT [31] (for an analytical illustration of the method in the case of normal statistics and with no azimuthal dependence of N_0, see Ref. [32]). The results are given in Table II. The values of χ_t^2 are strong indications that the polarimeter response was well understood both for the Saturne and the Bates data. To show the quality of the fit, Eq. (17) can be summed over the 12 φ bins to yield

$$\mathcal{N}(\theta) \simeq k\mathcal{N}_0(\theta)[1 + t_{20}T_{20}(\theta)] , \tag{19}$$

with the notation $\mathcal{N}(\theta) \equiv \sum_{\varphi\ \rm bins} N(\theta,\varphi)$; the equality holds only if N_0 is φ symmetric. Figure 6 illustrates the comparison between the Bates data and the fitted distribution $\mathcal{N}$. For negative t_{20}, the behavior of the analyzing power T_{20} has the effects of enhancing the yield for the angular region 100°–135° and reducing it in the region 135°–160°. The enhancement and reduction in the yield of the Bates data relative to the unpolarized interpolated calibration data can be clearly seen in Fig. 6. Furthermore, for the two points at $Q = 4.22$ and 4.62 fm^{-1}, the interpolated calibration data are the *same* (except for very small changes due to different FE distributions). The change of shape of the Bates data between these two points is visible and translates into t_{20} (4.62 fm^{-1}, 76.7°) $-$ t_{20}(4.22 fm^{-1}, 78.7°) $= 0.41$ with a systematic error due only to the knowledge of the analyzing power T_{20} and with a statistical error easily deduced from Table II. In other words, the slope of t_{20} as a function of Q can be seen here, independently of most systematic errors affecting the normalization.

Systematic uncertainties in t_{kq} may result from: (i) the interpolated calibration data N_0 obtained from the Monte Carlo (MC) simulation, (ii) the analyzing powers T_{kq}, and (iii) the Bates data $N_{\rm exp}$. The systematic uncertainties due to parameters used in the MC code were estimated by generating new interpolated calibration data for different values of a particular parameter within reasonable limits, keeping the values of the other parameters fixed. The tensor moments t_{kq} were then extracted using the new interpolated calibration data, and their difference from the nominal t_{kq} was taken as the systematic uncertainty due to that particular parameter. The proce-

TABLE III. Systematic errors in the tensor moments. Only the separate contributions to systematic uncertainties in t_{20} are shown. The first five uncertainties come from the generation of the interpolated calibration data and analyzing powers. The next three originate from the analysis of the Bates data. The total uncertainties result from a sum in quadrature of individual contributions.

Source	Uncertainty in t_{20} at $Q=$		
	3.78 fm^{-1}	4.22 fm^{-1}	4.62 fm^{-1}
Central energy of incident deuteron ±3 MeV	0.05	0.04	0.04
Energy spread of incident deuteron ±7 MeV	0.01	0.02	0.02
Upstream positions of CWC's ±0.5 cm	0.02	0.04	0.04
Downstream positions of CWC's ±1 cm	0.06	0.03	0.03
Interpolated T_{20}	0.05	0.03	0.03
z vertex cut ±3 cm	0.03	0.05	0.08
$E_{\rm diff}$ cut ±2 MeV	0.03	0.04	0.07
6.1 cm chamber cut ±1 cm		0.04	0.02
Statistical uncertainty in T_{20}	0.02	0.01	0.01
Absolute beam polarization at Saturne	0.04	0.03	0.01
Total systematic uncertainty in			
t_{20}	0.11	0.11	0.13
t_{21}	0.10	0.08	0.07
t_{22}	0.06	0.04	0.04

dures for determining the other sources of errors [points (ii) and (iii) above] were similar, but this time changing only the T_{kq} and $N_{\rm exp}$, respectively. The results for the systematic uncertainties in t_{20} are tabulated in Table III. The total systematic uncertainties from different sources for each Q point were combined in quadrature and are also given, for the three tensor moments t_{kq}, in the table.

The t_{21} and t_{22} results at $Q = 3.68$ fm^{-1} appear to be inconsistent with the rest of the data, being two standard deviations away from expectations (see Sec. V). This was traced to an abnormally high number of counts in two consecutive φ bins (60°–120°). No plausible explanation was found for this effect, but it was checked that the determination of t_{20} was not affected, since this anomaly did not reflect itself in the θ distribution.

IV. DETERMINATION OF THE CHARGE FORM FACTORS

As mentioned above, the magnetic dipole form factor G_M can be extracted directly from cross-section measurements. t_{20} and the longitudinal structure function A provide two different combinations of G_C, G_Q, and G_M, and can be used to separate the monopole and the quadrupole form factors. The three equations (9)–(11) may be inverted to solve for the deuteron form factors in terms of A, B, and t_{20}. Since these equations are quadratic, they admit, in general, two solutions. The normalization conditions (14) and a requirement of continuity in the slope of the form factors at the point where the two solutions cross ($x = 1$) were imposed to select the proper solution. A small complication arises when measured t_{20} points lie outside the physical region, a quite probable situation in the vicinity of the minimum of t_{20}: the solutions of the system then yield unphysical, complex values of the form factors.

The separation of the deuteron form factors was then performed for each Q value by minimizing [31] the quantity

$$\chi^2_G = \left[\frac{A^p - A(G_C, G_Q, G_M)}{\Delta A}\right]^2 + \left[\frac{B^p - B(G_M)}{\Delta B}\right]^2 + \left[\frac{t^m_{20} - t_{20}(G_C, G_Q, G_M, \theta_e)}{\Delta t_{20}}\right]^2, \quad (20)$$

where A^p and B^p are obtained from parametrizations [33] of the world data for these structure functions, and t^m_{20} are the measured values of the tensor polarization; ΔA, ΔB, and Δt_{20} (statistical and systematic uncertainties added in quadrature) are the corresponding uncertainties. Note that our parametrization of A [33] gives a very small weight to the SLAC data [1] which would favor a 40% higher value at our highest Q point. The two other tensor moments t_{21} and t_{22} determined in this experiment were not used in this calculation because they do not constrain significantly the final results. Once the individual form factors were determined, the quantities $\tilde{t}_{20}$ and $t_{20}(\theta_e = 70°)$ were calculated from Eqs. (16) and (11) for the sake of comparison of our results with previous data and with theory. Here again, a special procedure was necessary for data points lying outside the physical region: the amount by which the reconstructed quantities $\tilde{t}_{20}$ and $t_{20}(70°)$ extend beyond the physical limit was taken to be proportional to the amount by which the measured t_{20} extend beyond that limit. The result of this calculation, performed for our data points as well as for previous measurements (except for one point [6] because of its very large uncertainty), are given in Table IV. The errors in G_C and G_Q are greatly correlated because of the high precision in the measurement of A. Hence, for our last two points where $|G_C|$ is very small, the errors on G_Q come from the errors on A while the errors on G_C are mostly determined by the errors on t_{20} (the reverse is true at low values of Q).

In our four-momentum transfer range, the rise of t_{20} from its minimum toward zero is a consequence of the change of sign of G_C (Table IV), giving the first experimental evidence of the existence of a node in the charge monopole form factor. Using a polynomial fit to our G_C values, this node was located at $Q = 4.39 \pm 0.16$ fm^{-1}.

V. COMPARISON WITH THEORY

Much theoretical work has been devoted to the calculation of the deuteron electromagnetic form factors. Whether the interest lies in determining the neutron-proton force that binds the deuteron, extracting the poorly known electric form factor of the neutron, testing descriptions of the meson-exchange currents (MEC), seeking evidence for other degrees of freedom such as nu-

TABLE IV. Calculated values of the three deuteron form factors, $\tilde{t}_{20}$ and $t_{20}(70°)$ corresponding to all t_{20} measurements (statistical and systematic errors added in quadrature) to date, and using parametrizations A^p and B^p of the structure functions.

Q (fm^{-1})	A^p	B^p	G_C	G_Q	$\tilde{t}_{20}$	$t_{20}(70°)$	Ref.
0.988	$(3.11\pm0.05)\times10^{-1}$	$(3.53\pm0.18)\times10^{-3}$	0.550 ± 0.007	31.4 ± 14.4	-0.30 ± 0.14	-0.30 ± 0.14	[4]
1.353	$(1.45\pm0.02)\times10^{-1}$	$(3.26\pm0.16)\times10^{-3}$	0.377 ± 0.003	6.85 ± 2.68	-0.18 ± 0.07	-0.18 ± 0.07	[4]
1.74	$(6.20\pm0.09)\times10^{-2}$	$(2.42\pm0.12)\times10^{-3}$	0.242 ± 0.002	6.13 ± 0.90	-0.41 ± 0.06	-0.41 ± 0.06	[3]
2.03	$(2.98\pm0.04)\times10^{-2}$	$(1.76\pm0.09)\times10^{-3}$	$0.163^{+0.003}_{-0.004}$	4.43 ± 1.02	-0.59 ± 0.14	-0.58 ± 0.13	[3]
2.49	$(9.21\pm0.17)\times10^{-3}$	$(9.52\pm0.48)\times10^{-4}$	$0.0867^{+0.0029}_{-0.0039}$	2.16 ± 0.50	-0.79 ± 0.18	-0.75 ± 0.16	[5]
2.93	$(3.09\pm0.06)\times10^{-3}$	$(4.78\pm0.24)\times10^{-4}$	$0.0340^{+0.0127}_{-0.0251}$	$1.84^{+0.50}_{-0.65}$	-1.40 ± 0.37	-1.26 ± 0.32	[5]
3.78	$(5.33\pm0.21)\times10^{-4}$	$(1.02\pm0.05)\times10^{-4}$	$0.0127^{+0.0047}_{-0.0056}$	$0.482^{+0.077}_{-0.116}$	-1.45 ± 0.18	-1.23 ± 0.18	this work
4.22	$(2.37\pm0.13)\times10^{-4}$	$(4.14\pm0.25)\times10^{-5}$	$0.00166^{+0.00161}_{-0.00142}$	$0.315^{+0.010}_{-0.011}$	-0.92 ± 0.18	-0.83 ± 0.16	this work
4.62	$(1.21\pm0.08)\times10^{-4}$	$(1.69\pm0.12)\times10^{-5}$	$-0.00147^{+0.00106}_{-0.00104}$	$0.189^{+0.007}_{-0.008}$	-0.42 ± 0.21	-0.41 ± 0.18	this work

cleon resonances or quarks as constituents of the nucleus, understanding relativistic effects as nucleons move closer together, or reaching at asymptotically high momentum transfer the perturbative regime of quantum chromodynamics, the variety of theoretical approaches reflects both the richness and the complexity of the problem. A recent review has been given by Mazufarov *et al.* [34]. Many different model calculations have been developed to try to describe the A structure function as measurements have been performed to very high momentum transfer [1]. The observation of the first diffraction minimum in $B(Q)$ at $Q \simeq 7.2$ fm^{-1} [2] provides severe constraints on all models. Recently, high precision measurements of $A(Q)$ in the low momentum transfer region [35] have been used to lower the uncertainty on the neutron electric form factor and showed some evidence for relativistic effects even at $Q \simeq 3$ fm^{-1}. The data from this experiment allow for the first time a significant comparison with the individual charge form factors. For this comparison, the different models will be classified as in Ref. [2]: nonrelativistic impulse approximation (NRIA), meson-exchange currents (MEC) and isobar configurations (IC), relativistic impulse approximation (RIA), hybrid quark-hadron models, Skyrmion models, and perturbative quantum chromodynamics (PQCD).

A. Nonrelativistic impulse approximation

In the impulse approximation, the virtual photon exchanged between the electron and the deuteron interacts with individual nucleons within the nucleus, and the electromagnetic form factors of the nucleons are assumed to be the same as for free nucleons. This last hypothesis was recently discussed and found reasonable [36]. Nonrelativistically, the coupling of the photon to the charges yields for G_C, G_Q, and part of G_M a product of the isoscalar nucleon electric form factor with an integral of the S and D-state wave functions, while its coupling to the nucleon spins adds to G_M a contribution proportional to the isoscalar nucleon magnetic form factor. The analytic expressions for the deuteron form factors in the NRIA may be found in many references [2,8–13]. Even though the NRIA is not expected to give an exact result, its description is fair enough up to $Q \simeq 4$ fm^{-1} to investigate in this approximation the effect of various nucleon-nucleon (NN) potentials and of various parametrizations of the poorly known neutron electric form factor G_E^n.

In the NRIA, $G_C(Q)$ has a structure very similar to $u(k)$, the S-state wave function in momentum space, with k, the momentum of the nucleons with respect to their center of mass, equal to $Q/2$ [7]. The weaker the short-range repulsion of the NN potential, the more the node of $u(k)$ and $G_C(Q)$ will move to higher values, and the less steep the slope of t_{20} will appear. At the limit where the hard core disappears, the node moves to infinity and $\tilde{t}_{20}$ remains lower than $-1/\sqrt{2}$. NN potentials developed in the last ten years (among others Paris [37], Argonne v_{14} [38], and Bonn [39]), all incorporate the main features of the NN scattering data. But phase-shift equivalence does not imply equal potential or wave function, and therefore differences may manifest themselves in the deuteron form factors. In the case of the so-called full Bonn potential (Bonn-E) [39], the calculation must take care of its explicit energy dependence; this was done by Pauschenwein *et al.* [40] by applying to the original wave function ψ_E the Perey transformation $\psi_S = (1-\partial V/\partial E)^{1/2}\psi_E$, which is an effective way of carrying out the necessary modification of the current operator (see also Ref. [41]). As for the energy-independent versions of the Bonn potential (Bonn-Q, Bonn-R) [39], Desplanques argued that they should not have been derived with the requirement to reproduce as much as possible the D-state probability of the full model and cautioned about their use wherever the deuteron D wave is involved [41], which is certainly the case for t_{20}. Calculations of the deuteron form factors and e-d observables in the NRIA have been performed by many authors [40,42–46], and some are shown in Fig. 7. It is remarkable that the NRIA gives a good description of the data at these intermediate momentum transfers.

Desplanques and Amghar [47] recently explored the possibility that some of the NN interaction models may be equivalent up to a unitary transformation. Quantities where the NN system couples to an external probe

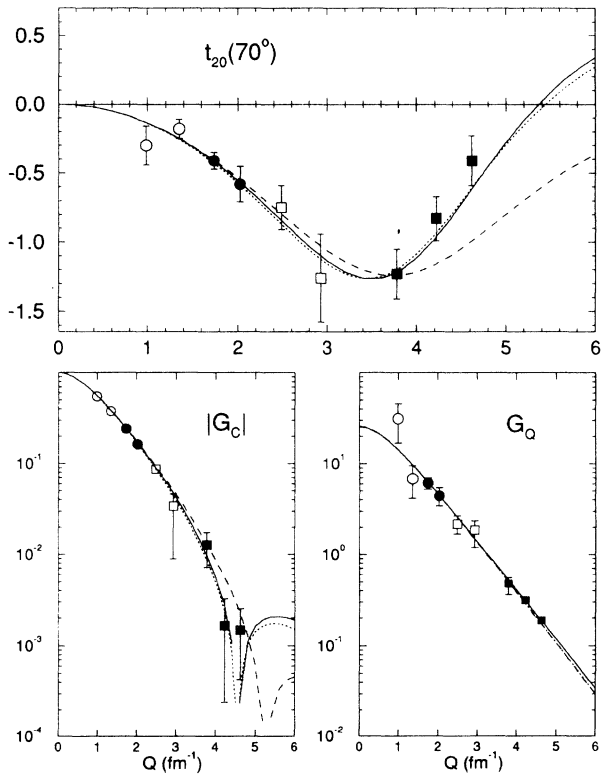

FIG. 7. $t_{20}(\theta_e = 70°)$, G_C, and G_Q calculated in the NRIA, using the Höhler nucleon form factors [50]. Solid line from Ref. [45] using the Paris potential, dotted line from [46] with the Argonne v_{14} potential, dashed line from [40] with the full Bonn-E potential. Data points have been extracted from t_{20} measurements as explained in Sec. IV and in Table IV: open circles [4], filled circles [3], open squares [5], filled squares [this work]. Note that, for our data point at $Q = 4.62$ fm^{-1}, G_C is calculated to be negative (within statistical errors).

are affected by this transformation and should therefore be corrected accordingly. Once this is done, predictions made from different models tend to move closer to each other.

Using a dispersion relation approach, Muzafarov and Troitskii [43] calculated a deuteron wave function directly from the NN scattering phase shifts. Their results for the deuteron form factors in NRIA are very close to calculations based on NN potentials. Locher and Švarc [48] determined the d-p-n vertex function by a fit to the e-d observables A and B. Because this calculation is performed within NRIA and presupposes that no correction to NRIA is needed, its validity may be questionable. Nevertheless, within their model, their fit of B was improved when the recent Saclay data on A [35] were excluded from the data set, while our data are in favor of their t_{20} prediction when the same Saclay data are included in the fit (dashed curve of Fig. 4 in [48]).

Because of the above-mentioned factorization, the isoscalar nucleon electric form factor cancels in the ratio x and therefore in $\tilde{t}_{20}$ [see Eqs. (15)–(16)]. In the NRIA, $\tilde{t}_{20}$ is strictly independent of G_E^n. Because its magnetic contribution is small, t_{20} is nearly independent of G_E^n. The dependence of the individual form factors on G_E^n is illustrated in Fig. 8. This behavior may be seen in all models which go beyond the NRIA [17]. Note that the parametrization of Ref. [52] is not supported by new measurement of G_E^n [53].

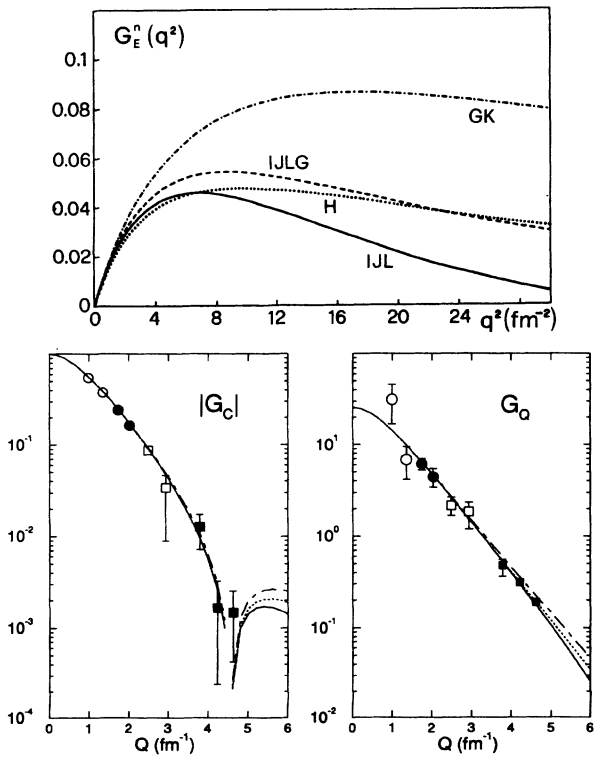

FIG. 8. G_E^n, G_C, and G_Q calculated in the NRIA for different nucleon form factors: Refs. [49] (solid curve), [50] (dotted), [51] (dashed), and [52] (dot-dashed). The G_E^n figure and the calculations are from Ref. [45]. See Fig. 7 for data legend.

B. Meson-exchange currents and isobar contributions

Isoscalar meson exchange and the resulting additional coupling of the virtual photon to the deuteron are most easily depicted by the Feynman diagrams of Fig. 9. The most commonly used prescription to calculate the contributions of isoscalar MEC's to the deuteron form factors is given by Gari and Hyuga (GH) [54] who derived MEC operators using a perturbative approach to evaluate these diagrams. Meson-nucleon vertex form factors and the large width of the ρ meson are important features included by GH in their MEC formalism. For the pair and retardation (recoil+reorthonormalization) currents, the pion contribution largely dominates over that of heavier mesons. In contradistinction with isovector exchange currents where the photon can couple directly to a pion in flight (thus leading to a very large contribution in some cases), the total number of pion lines at the photon vertex may only be odd in an isoscalar system because of G parity. The $\rho\pi\gamma$ and $\omega\sigma\gamma$ diagrams are equivalent to three- and five-pion contributions and must be considered when calculating the deuteron form factors.

Exchange current operators should be constructed to obey the continuity equation $\nabla \cdot \mathbf{J} + i[H, \rho] = 0$, where $\mathbf{J}$ and ρ are the current and charge operators of the system. Whenever the commutator of the NN potential and of the single nucleon charge operator does not vanish, a corresponding contribution to the two-body or exchange current operator $\mathbf{J}$ must exist to fulfill the continuity equation. This method however is not a complete procedure in the sense that exchange current operators which have a transverse character are not constrained by the continuity equation, and therefore by the NN interaction: they are model dependent. The $\rho\pi\gamma$ MEC is an example of a model-dependent exchange current. Most MEC calculations include various relativistic one- and two-body current contributions (RC) added perturbatively to the NRIA results [55].

Figure 10 gives the results of some recent calculations of NRIA+MEC+RC [40,45,46,56]. As compared with NRIA (Fig. 7), the minimum of G_C is shifted to some-

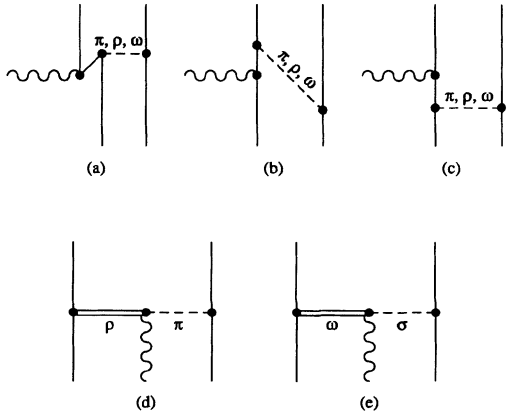

FIG. 9. Meson exchange diagrams: (a) pair term, (b) recoil, (c) reorthonormalization, (d) $\rho\pi\gamma$, (e) $\omega\sigma\gamma$ (so far taken into consideration only in Refs. [66,56,71]).

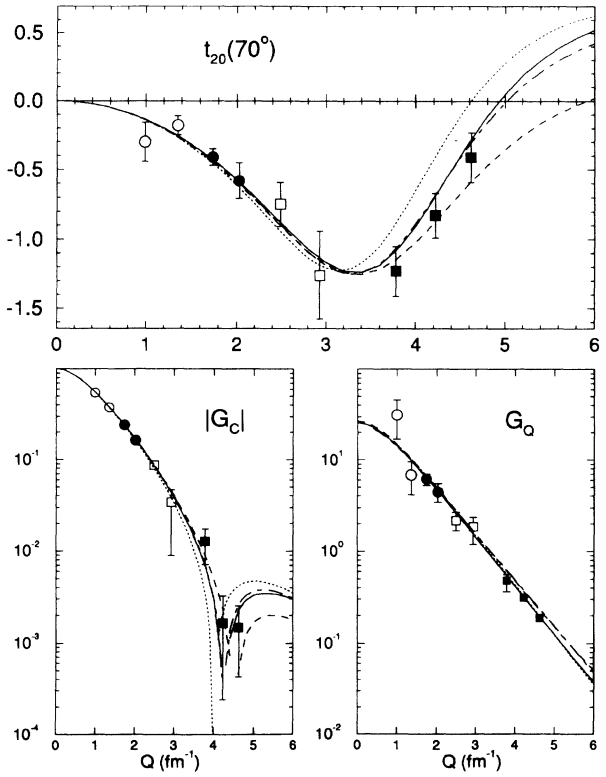

FIG. 10. $t_{20}(70°)$, G_C, and G_Q calculated in the NRIA+MEC+RC, using the Höhler nucleon form factors [50]. Solid line from Ref. [45] using the Paris potential, dotted line from [46] with the Argonne v_{14} potential, and dashed line from [40] with the full Bonn-E potential. The dot-dashed curve includes isobar configurations [60]. See Fig. 7 for data legend.

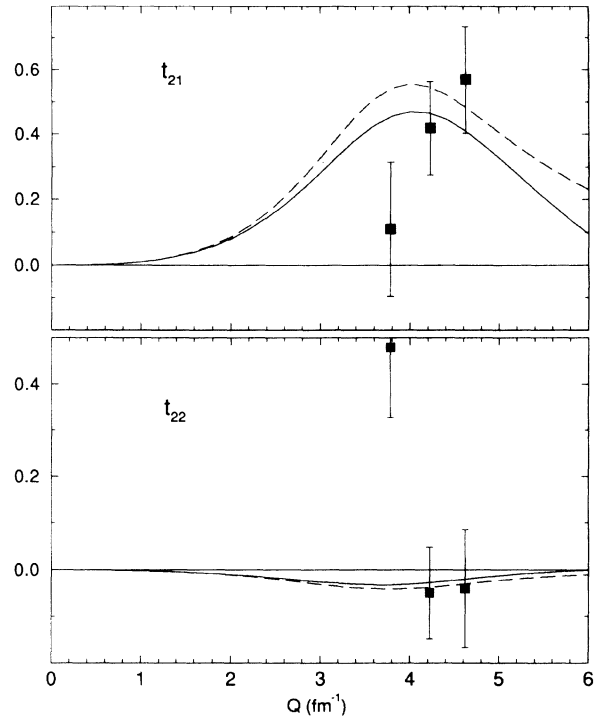

FIG. 11. t_{21} and t_{22}. Our data are not corrected for different electron angles (see Table II). The calculations were performed for $\theta_e = 78.7°$ using the form factors of Ref. [45], NRIA (dashed curve), NRIA+MEC+RC (solid curve).

what lower Q values, as was noted by earlier calculations [11,42,54,57]. In most recent calculations, this shift is larger than our data would suggest, except in the case where the Bonn-E potential is used [40] and in the calculation of Ref. [45]. In the latter however, the authors use a lower value (0.4) for the coupling constant $g_{\rho\pi\gamma}$ than commonly accepted (0.56) and neglect the width of the ρ. This trend is in apparent contradiction with similar calculations in the three-body system where the isoscalar charge form factor extracted from e-^{3}He and e-^{3}H elastic scattering [58] is better reproduced with the same MEC contributions as used for the deuteron [59].

Figure 11 illustrates our results for t_{21} and t_{22}, together with the corresponding predictions using the deuteron form factors calculated in Ref. [45].

Using a nonrelativistic reduction of current operators in the framework of a one-boson exchange (OBE) model, a more complete investigation of relativistic effects on e-d scattering was performed by Tamura *et al.* [56], consistently with the treatment of MEC. This calculation includes not only the above-mentioned relativistic corrections to the nuclear current but also the Lorentz boost of the center of mass of the nucleus. The agreement with our data is excellent. Completely relativistic calculations along the same line will be discussed in the next section.

Isobar degrees of freedom may be taken into account by adding to the wave function explicit $\Delta\Delta$ and NN^* components. The complete deuteron wave function is obtained by solving a set of equations which express the coupling between these channels and the np channel (coupled channels). The deuteron form factors are then modified, both in the NRIA, with the assumption that the isobars have form factors proportional to those of the nucleons, and in the MEC calculation where additional terms must be taken into account. One model [60] with very small isobar admixtures (0.36% distributed among four $\Delta\Delta$ channels) is in good accord with the data (Fig. 10). Another one [61] is derived within an R-matrix formalism: outside a boundary radius r_0, the deuteron is modeled as a mixture of baryon-baryon configurations, with a boundary condition at r_0 originating from an assumed six-quark configuration inside the sphere of radius r_0. Within this calculation, the model with $r_0 = 0.74$ fm lies above the data and is almost indistinguishible from the dotted curve in Fig. 10. Increasing the radius to 1.05 fm increases the amount of $\Delta\Delta$ components from 1.8 to 7.2% and worsens the agreement with our data. Another coupled-channels calculation based on the separable Graz II potential [62] yields 0.8% $\Delta\Delta$ components in the deuteron and reproduces our data.

C. Relativistic impulse approximation

Relativistic covariant calculations of the deuteron form factors can be divided into two general approaches: "in-

stant form" and "front form," corresponding to two allowed forms of the representation of the Poincaré group (choice of the infinitesimal generators) [63]; for each case the dynamics depend on the choice of the kinematic components of the four-momentum variable. Relativistic calculations based on the Bethe-Salpeter equation (BSE) are of the instant-form type while the front-form approach (also called light-front quantum mechanics) is a type of Hamiltonian dynamics for a fixed number of particles where the matrix elements of the nucleon current operator and the nucleon electromagnetic form factors are related by kinematic transformations. Most relativistic calculations do not include contributions from MEC's such as the $\rho\pi\gamma$ process and are therefore referred to as relativistic impulse approximation (RIA). However the pair and retardation currents are included automatically in some models of RIA [64,65]. A fully relativistic analysis of the $\rho\pi\gamma$ and $\omega\sigma\gamma$ currents, calculated consistently with the NN dynamics within a relativistic quasipotential one-boson-exchange model, has been done recently by Hummel and Tjon [66].

In order to achieve a manageable three-dimensional reduction of the BSE, various prescriptions have been used in the literature, leading to different quasipotential equations. The calculation of Arnold *et al.* [64] assumes that the spectator nucleon is on the mass-shell while the interacting nucleon is off-shell. The deuteron-neutron-proton vertex is then described by four invariants, two of which correspond to the usual S- and D-state wave functions. The other two invariants are the ^1P- and ^3P-state wave functions, which appear because of the existence of extra degrees of freedom when the virtual interacting nucleon is in a negative energy state. A parameter λ can be varied between 0 (pure pseudovector) and 1 (pure pseudoscalar) for the boson-nucleon couplings used to generate the wave function. Their results both for $B(Q)$ and t_{20} are in favor of pure pseudovector coupling, where the RIA is closer to the NRIA (see Fig. 11 of [64]).

Recently, Braun and Tokarev [67] undertook a similar calculation though with a different, allegedly more rigorous, treatment of the integrand in the form factor integrals. The agreement with t_{20} is however slightly worse (Fig. 12f of Ref. [67]).

Assuming that both nucleons are on the mass-shell, Krutov and Troitskiĭ [68] found very small relativistic corrections to t_{20}, about 7% at $Q = 4.5$ fm^{-1}.

Bhalerao and Gurvitz [69] used another prescription, constructing the wave function of the deuteron by a combination of two functions, corresponding respectively to the case where the spectator, or struck, nucleon is on-shell. This leads to a somewhat too small slope of t_{20}. The limit where only the spectator nucleon is on shell is in better agreement with the data, as in Arnold *et al.* [64].

Rupp and Tjon [70] obtained rigorous solutions of the BSE by using separable potentials. This class of potentials however, whether nonrelativistically (with the exception of [62]) or in their covariant generalizations, misses the general features of the charge form factor: the node is shifted to Q values of about 5.5 fm^{-1}, much higher than the experiment.

Hummel and Tjon [66] have performed a relativistically covariant analysis of $\rho\pi\gamma$ and $\omega\sigma\gamma$ MEC's, which were treated consistently with the NN dynamics within a quasipotential one-boson-exchange (OBE) model. The perturbative treatment of MEC's in the nonrelativistic approach neglects the recoil corrections due to the kinetic energy of the nucleons. This approximation is not justified at high momentum transfers. Hummel and Tjon derived the relativistic formulas for the $\rho\pi\gamma$ and $\omega\sigma\gamma$ current operators and evaluated their matrix elements using a relativistic OBE model with π, ρ, ω, σ, η, and δ mesons. To do so, they resorted to a quasipotential approximation where the nucleons are treated on equal footing, by putting them equally far off the mass shell and setting the relative energy variable equal to zero. They find the $\rho\pi\gamma$ contribution to the form factors to be much smaller than in the nonrelativistic case, and consequently the $\omega\sigma\gamma$, thus far never considered, is of comparable importance. Their results are displayed on Fig. 12. The RIA is seen to be in excellent agreement with the data, while the addition of the MEC changes the results by less than one experimental error bar. The $\rho\pi\gamma$ and $\omega\sigma\gamma$ contributions to G_Q almost exactly cancel each other, while the $\omega\sigma\gamma$ contribution to G_C is twice as large, with opposite sign, as the $\rho\pi\gamma$ one. Similar relativistically covariant calculations have been performed by Devine [71], with equally good agreement with our data. In this work, it is noted that the zero relative energy quasipoten-

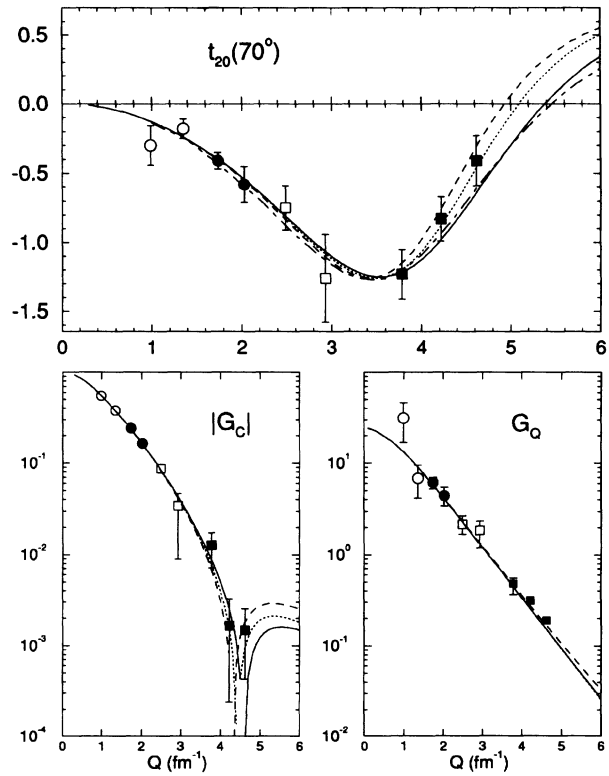

FIG. 12. $t_{20}(70°)$, G_C, and G_Q in two relativistic calculations; from [66]: RIA (dotted curve), RIA+$\rho\pi\gamma$ (dashed curve), RIA+$\rho\pi\gamma$ + $\omega\sigma\gamma$ (solid curve); the dot-dashed curve is RIA in light cone formalism from [72], using the Argonne v_{14} potential. Both calculations use the H nucleon form factor [50]. See Fig. 7 for data legend.

tial constraint is inconsistent when used for both initial and final deuterons. Calculations using different approximations show small differences for $\rho\pi\gamma$, $\omega\sigma\gamma$, and $\omega\eta\gamma$ MEC's, but significant differences for the RIA form factors. A formalism based on the consistent zero relative energy constraint in the Breit frame has been derived and calculations based on this formulation are in progress.

Relativistic models of front-form use the four-vector $(t\pm z, x, y)$ as the kinematic variable, the four-momentum being then $(E \pm p_z, p_x, p_y)$. The equation of motion has a form similar to that of the nonrelativistic Schrödinger equation, with a relativistic wave function of the deuteron related to the nonrelativistic one in a simple way: $\psi_{\rm rel}(k) = (k^2 + M_d^2)^{1/2}\psi_{\rm nonrel}(k)$. The t_{20} predictions in the light-cone or light-front quantum mechanics as calculated by Chung *et al.* [72] are shown in Fig. 12. Six different potentials were used in this calculation. The results for t_{20} using the Reid soft core (RSC), Argonne v_{14}, and Paris potentials are in better agreement than those using any of the Bonn potentials (see however above remarks and Refs. [40,41]). There are larger differences in G_C than in G_Q among the three Bonn potentials. Frankfurt *et al.* [73] performed a similar calculation using the Paris potential and their result is very close to the result of Chung *et al.*

D. Quark-hadron hybrid models

When electron scattering involves higher momentum transfers, the deuteron is probed at smaller internucleon distances. The quark substructure of the nucleons should then manifest itself in observables, but a distinct signature of quark effects in nuclei is still very elusive. Some calculations of the deuteron electromagnetic form factors explicitly take into account quark degrees of freedom. The deuteron structure is then described in hybrid models which mix quark and nucleon degrees of freedom.

The first class of such models assumes for the deuteron wave function a sum of two wave functions, a conventional NN wave function and a six-quark ($6q$) configuration, but does not contain any dynamics to link the hadronic and the $6q$ components. Kobushkin and Shelest [74] write $\psi_d = \alpha\psi_{np} + \beta\psi_{6q}$, where ψ_{np} is calculated from the Reid hard core potential while ψ_{6q} is determined using a relativistic oscillator quark model. The six quarks are all considered to be in an S state. The oscillator constant and the probability of the $6q$ admixture β^2 were determined by fitting the then available data on A and B. They obtained $\beta^2 = 2.5\%$, but the $6q$ contribution to G_C is so large and positive that the node of this form factor disappears. This is in clear contradiction with our data. Burov and Dostovalov [75] had a similar approach, with the difference that the $6q$ component was restricted to a small sphere of radius 1 fm and that MEC contributions (at the nucleon level) were included in the calculation of the form factors. Their $6q$ admixture was 3.5% and G_C is also without a node (Fig. 13). Cheng and Kisslinger [76] took into account five different six-quark configurations, also within the relativistic oscillator quark model. Their result differs widely from the work in Refs. [74,75], since they do predict a node in G_C in the right Q range. Within these models, the form factors thus seem to be very sensitive to the $6q$ configurations being used.

A smooth dynamical connection between the configuration of two three-quark baryon clusters at long distances and a $6q$ configuration at short distance may be provided within the nonrelativistic quark-cluster model (QCM), using the resonating group method. The QCM is able to reproduce the repulsive nature of the NN interaction at short distances, but the intermediate range attraction is included through two-pion exchange or a phenomenological σ exchange. The long-range part of the interaction is given by OPEP between quarks. Yamauchi and Wakamatsu [77] demonstrated that it is rather ambiguous to speak about the $6q$ components in the deuteron independently of their relation to the NN component. They found that the $(0s)^6$ $6q$ contribution to the form factors is largely canceled by that of part of the S-wave NN term (the interference is here crucial) and calculate e-d observables which are very close to the NRIA. Only in the magnetic form factors do quark effects manifest themselves through the antisymmetrization of quarks between the two clusters. Ito and Faessler [78] and Ito and Kisslinger [79] (Fig. 13) investigated quark exchange contributions to the form factors: the impulse one-body current operators consist of a direct

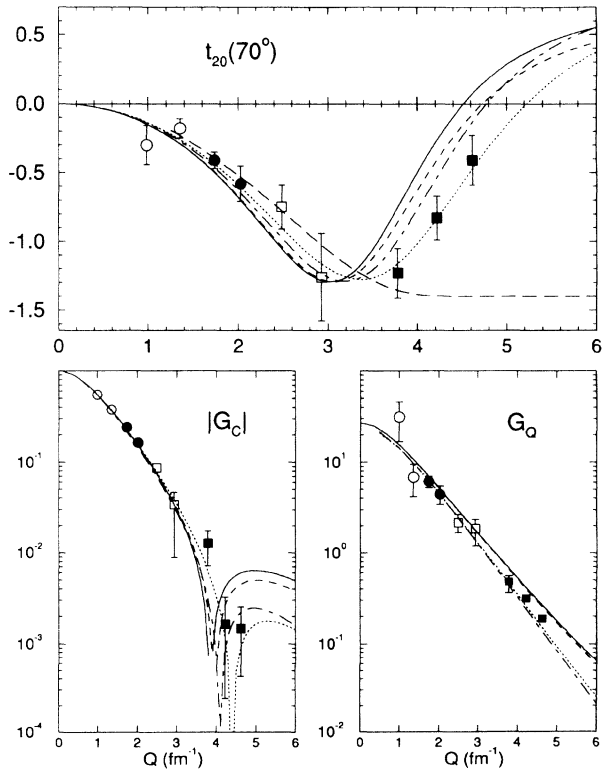

FIG. 13. $t_{20}(70°)$, G_C, and G_Q as predicted by quark models. From Ref. [80], NRIA+π-pair MEC (dashed curve), same+quark interchange (solid curve); from Ref. [79], with quark cluster size 0.50 fm (dotted curve) and 0.55 fm (dot-dashed curve). The long-dashed curve corresponds to the prediction of Ref. [75] for $\tilde{t}_{20}$. See Fig. 7 for data legend.

term (the coupling of the virtual photon to a quark in a cluster) and two exchange terms, where two quarks from different clusters are interchanged (the virtual photon then couples either to a spectator quark or to an interchanged quark). They get a reasonable description of the observables in our four-momentum transfer range. The connection between antisymmetrization in [77] and quark exchange in [78,79] is not completely clear. Buchman *et al.* [80] improved such calculations by including contributions from two-body pion and gluon exchange currents on the quark level. Quark exchange is found to have a small effect on t_{20}, so that, as in conventional calculations, the model of G_C is shifted to lower values of Q because of the π pair contribution (Fig. 13).

Six-quark and hadronic configurations may also be linked in an R-matrix formalism through a boundary condition matching the wave functions at a given radius. The above-mentioned work of Blunden *et al.* [61] did not examine the contribution of the $6q$ components to the form factors. This was done by Dijk and Bakker [81]: the $6q$ component of ψ_d was parametrized and adjusted to fit the structure functions A and B. Their prediction for t_{20} is in good agreement with our data.

E. Skyrmion model

In the Skyrme model [82], baryons are identified with soliton solutions (Skyrmions) of a Lagrangian constructed on an SU(2) field $U(\mathbf{r}) = \exp[i\boldsymbol{\tau}\cdot\hat{\mathbf{r}}\vartheta(r)]$. τ is the nucleon isospin operator and $\vartheta(r)$ is called the chiral angle, a function which satisfies an equation of motion of the underlying Lagrangian. The isoscalar electromagnetic current operator J^μ is proportional to the anomalous baryon current operator B^μ, which depends on the fields $\mathbf{U}$ of the Lagrangian but not on their interaction:

$$J^\mu = \frac{1}{2}B^\mu = \frac{\varepsilon^{\mu\nu\alpha\beta}}{48\pi^2}\mathrm{Tr}[U^\dagger\partial_\nu UU^\dagger\partial_\alpha UU^\dagger\partial_\beta U] \ . \quad (21)$$

Nyman and Riska [83] predicted the deuteron electromagnetic form factors within the Skyrme model with the following assumptions: $\vartheta(r)$ was not derived from an explicit Lagrangian model, but adjusted to reproduce the isoscalar nucleon form factor. To represent the deuteron, a product *ansatz* of two soliton fields was used:

$$U(r_1, r_2; r) = U(r - r_1)U(r - r_2) \ , \quad (22)$$

where r_1 and r_2 are the coordinates of the centers of the two solitons and r is the point of interaction with the electromagnetic field. Inserting Eq. (22) into Eq. (21), the current operator for the deuteron can be expressed as a sum of one- and two-body operators:

$$J^\mu(r_1, r_2; r) = J^\mu(r - r_1) + J^\mu(r - r_2) + J^\mu_{\mathrm{exc}}(r_1, r_2; r) \ , \quad (23)$$

where $J^\mu(r - r_i)$ is the isoscalar current operator of single nucleons and J^μ_{exc} is an irreducible two-body exchange current operator. This exchange current in the Skyrme model has been formally identified [84] with the conventional $\rho\pi\gamma$ MEC. The extended structure of the nucleons is taken into account automatically in the construction of the operators, so that no phenomenological cutoff form factors at the meson-nucleon vertices are needed. Nyman and Riska did not introduce any dynamics in the Skyrme model: the deuteron wave functions needed to calculate the matrix elements of the current operator J^μ must be taken from another dynamical model, and they chose to use the wave function generated conventionally from the Paris NN potential (the differences in the predicted form factors when using the RSC potential are small). Their results are shown in Fig. 14 to be in fair agreement with our data. As is the case for the conventional nonrelativistic results, the minimum of G_C is shifted to lower momentum transfer with respect to that of the IA result. However, the contribution of the two-body exchange current operator has a larger effect on the calculated G_Q.

Braaten and Carson [85] consider the previous result fortuitous: they criticized the product *ansatz* of Eq. (22) and the resulting additivity of the current operators. They calculated the deuteron form factors in the Skyrme model under the assumption that the deuteron should be identified with the ground state of the toroidal $B = 2$ Skyrmion. All three form factors are then overestimated by an order of magnitude.

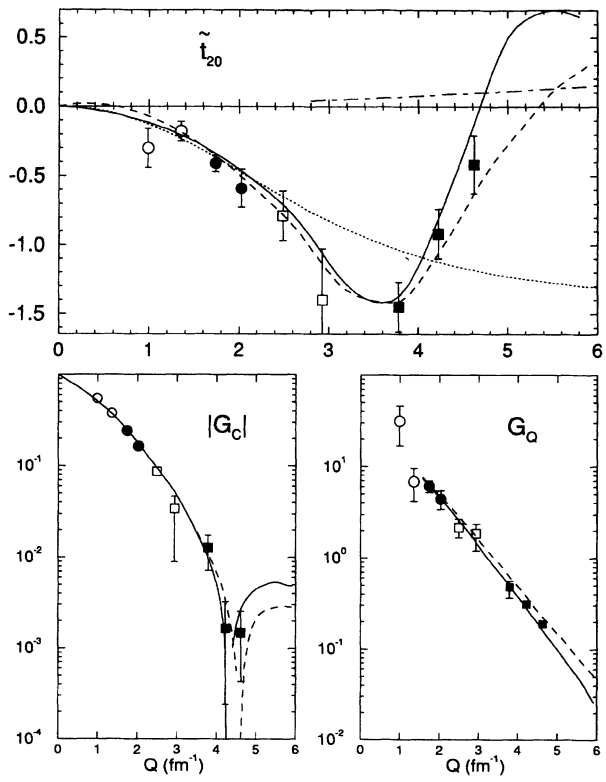

FIG. 14. $\tilde{t}_{20}$, G_C, and G_Q in a Skyrme model [83]: IA with Paris potential (dashed curve), IA+exchange currents (solid curve); the chiral angle is obtained using the nucleon form factor from [52]. $\tilde{t}_{20}$ from PQCD predictions: Eq. (25) [88] (dotted curve), and Eq. (26) [89,90] (dot-dashed curve). See Fig. 7 for data legend.

F. Perturbative quantum chromodynamics

At sufficiently large momentum transfer, PQCD is expected to become applicable. In elastic scattering, the deuteron keeps its identity, so that it is generally assumed that the momentum transfer is shared among the six quarks. Brodsky and collaborators [86] studied the high-Q behavior of the electromagnetic form factors of hadrons and of the deuteron within the framework of PQCD. Using the above assumption, they derived the so-called quark counting rule which predicts for the deuteron $\sqrt{A(Q)} \propto Q^{-10}$ as $Q \to \infty$.

Carlson and Gross [87] showed that, though classical nuclear physics may lead to the same power law, spin observables could provide a distinctive signature of the validity of PQCD: working in a helicity basis, the dominant matrix element of the electromagnetic current is the one where the deuteron has a 0 helicity in both initial and final states. This corresponds to a longitudinal form factor

$$G_{L,00} = -\sqrt{Q^2 + 4M_d^2}[G_C + \tfrac{4}{3}\eta G_Q]$$

which exhibits a Q^{-9} asymptotic behavior. The double helicity flip term

$$G_{L,+-} = \sqrt{Q^2 + 4M_d^2}[G_C - \tfrac{2}{3}\eta G_Q]$$

is suppressed by a factor Q^2 compared to $G_{L,00}$, which leads, using Eqs. (15) and (16), to the prediction:

$$\lim_{Q \to \infty} \tilde{t}_{20} = -\sqrt{2} \, . \tag{24}$$

Carlson [88] later suggested that this asymptotic behavior could be matched to the low transfer limit of Eq. (14) by the *ad hoc* construction:

$$G_C = (1/M_d^2 \mathcal{Q}_d + \tfrac{2}{3}\eta) G_Q \, . \tag{25}$$

Our data (Fig. 14) contradict this supposition and indicate that this momentum transfer range is still far from where PQCD is applicable.

Brodsky and Hiller [89] recently reexamined the question of asymptotic behavior of the deuteron form factors: the relevant transfer momentum scale for the validity of PQCD is claimed to be $Q \gg \sqrt{2M_d \Lambda_{\rm QCD}} \sim 4.5$ fm^{-1}, which is much lower than the scale usually given by $\eta \gg 1$. The energy scale $\Lambda_{\rm QCD}$ is taken to be around 200 MeV. A calculation of the form factors in the light cone formalism [89,90], keeping only the leading term $G_{L,00}$, leads to

$$G_C = (-1 + \tfrac{2}{3}\eta) G_Q, \quad \tilde{t}_{20} \simeq -\sqrt{2} \frac{\eta(\eta - 1)}{\eta^2 - \eta + \frac{3}{4}} \, , \tag{26}$$

which in the limit $\eta \gg 1$ leads to the Carlson and Gross prediction of Eq. (24). Our data are not incompatible with this behavior as of $Q \simeq 5$ fm^{-1} (Fig. 14), but the assumption of the dominance of $0 \to 0$ transition cannot account for the observed dip in the magnetic form factor [2].

VI. SUMMARY

In summary, the deuteron tensor polarization in elastic electron deuteron scattering has been measured up to a four-momentum transfer of 4.6 fm^{-1}. The first recoil tensor polarimeter to operate in the deuteron energy range of 100–200 MeV (AHEAD) was used for this purpose. The tensor moment t_{20}, together with the existing cross-section data, was used to perform the separation of the charge monopole and quadrupole form factors of the deuteron. The rise of t_{20} from its absolute minimum at $Q \simeq 3.5$ fm^{-1} towards zero around 5 fm^{-1} is related to the existence of a node in G_C which we can locate at $Q \simeq 4.4$ fm^{-1}. The two other moments t_{21} and t_{22} were determined as well, but with a lower precision: they are compatible with the other observables, but do not supply any new information on the deuteron electromagnetic structure.

Many models, or even classes of models, for the deuteron form factors are in fair agreement with our data. Only those models which do not predict a node in G_C, such as *naive* quark models, are clearly discarded. Not too surprisingly, our data also indicate that perturbative QCD is not applicable for this process in this intermediate momentum transfer region. In conventional nonrelativistic calculations, the MEC contributions (together with relativistic corrections) tend to shift the node of G_C towards too small values of Q. This is in apparent contradiction with the three-body isoscalar electric form factor which is well described by similar calculations. More precise measurements and a better understanding of the isoscalar meson exchange currents are needed to resolve this point. A small $\Delta\Delta$ admixture in the deuteron wave function, calculated using coupled channels equations, can improve the agreement with the data. Quark configurations may also be considered explicitly without affecting greatly the observables. Interestingly enough, the isoscalar exchange current can be calculated from a Skyrme model, without any free parameter but with some assumptions about the nature of a composite $B = 2$ Skyrmion. Relativistic calculations were until recently always performed within the impulse approximation. The first calculation of the deuteron form factors which evaluates consistently the meson exchange contributions within a relativistic one-boson-exchange model is one of the very few model calculations which reproduces all three observables t_{20}, A, and B. This is due in part to the $\rho\pi\gamma$ contribution which is found smaller than in nonrelativistic calculations, and to the introduction of the $\omega\sigma\gamma$ contribution.

This experiment is one of many others which could contribute to cutting the famous "Gordian" knot of the deuteron electromagnetic structure [91,54]: t_{20} in e-d scattering is not sensitive to the poorly known G_E^n, which in turn is being measured with new polarization techniques; the comparison of the $A = 2$ and $A = 3$ isoscalar form factors should lead to a better understanding of the hitherto more ambiguous isoscalar exchange currents; precision measurements of the structure functions A and B constrain the dynamical description of electron elastic scattering by showing evidence for relativistic effects,

even at moderate momentum transfers; breakup of polarized deuterons could contribute to unraveling the exact spin structure of the deuteron.

More precise data on the deuteron form factors are to be anticipated in the next few years: high precision measurements of A and B are planned; tensor polarization measurements using internal polarized targets in an electron ring are underway or proposed; and recoil polarimetry techniques are being improved, which will lead to experiments of the type discussed in this paper in order to gain precision in the region of the nod of G_C and to extend the measurements up to about 6.5 fm^{-1}.

APPENDIX

We illustrate formally how the Monte Carlo code generates the proper angular and energy weights and the interpolated calibration data. A proof of Eq. (17) is established.

The quantities that characterize the polarimeter are the analyzing powers T_{kq} and the efficiency ε. For a fixed $E_{\rm diff}$ cut, they both depend on the deuteron energy E (which itself depends on the deuteron energy at the entrance of the polarimeter $E_d^{\rm inc}$ and the vertex position Z) and on the polar scattering angle θ. The minimum set of variables $\{m\} = \{E, \theta\}$ would describe an ideal polarimeter. Because of the finite target size, ε (but not T_{kq}) depends also on $\{i\} = \{\rho, \psi, \theta^{\rm inc}, \varphi^{\rm inc}\}$, the position and angles of the incident deuteron, and on the azimuthal scattering angle φ. We denote by $\{v\} = \{m, i, \varphi\}$ the total ensemble of variables.

At the calibration, the incident beam has negligible energy spread ($E_d^{\rm inc} = \langle E_d^{\rm inc}\rangle \equiv E_d^{\rm pol}$). When scattering $N_{\rm cal}^{\rm inc}(i)$ unpolarized deuterons, the measured scattering yield

$$N_{\rm cal}(v) = N_{\rm cal}^{\rm inc}(i)\varepsilon(v) \tag{A1}$$

defines the efficiency ε.

In the Bates experiment, since the deuterons are tensor polarized, the count yield is [29]:

$$N_{\rm exp}(v) = N_{\rm exp}^{\rm inc}(E_d^{\rm inc}, i)\varepsilon(v)\mathcal{T}(m, \varphi) , \tag{A2}$$

where

$$\mathcal{T}(m, \varphi) = 1 + \sum_{q=0}^{2}(2 - \delta_{q0})t_{2q}T_{2q}(m)\cos q\phi .$$

ε is in effect proportional to a cross section and to a detector efficiency $A^{\rm MC}$ (which is accounted for by the Monte Carlo simulation) due mostly to absorption in the target:

$$\varepsilon(v) \propto \mathcal{W}(E)\sigma_E(\theta)A^{\rm MC}(v) . \tag{A3}$$

For each target Z slice, or E bin, insertion of Eq. (A3) into Eq. (A1) yields, after integration over the calibration FE event distribution and over φ:

$$N_{\rm cal}(m) \propto \sigma_E(\theta)\int\cdots\int N_{\rm cal}^{\rm inc}(i)A^{\rm MC}(v)d\{i\}d\varphi . \tag{A4}$$

Thus σ_E is defined as the effective cross section which, when folded in the Monte Carlo with the calibration incident deuteron distribution, generates the observed angular distribution of the calibration counts for this particular E bin [16].

Similarly for $\mathcal{W}(E)$, integration of Eq. (A4) over θ yields the distribution of calibration events along the target axis. The energy-weighting factors are then adjusted to reproduce these counts.

$\mathcal{W}(E)$ and $\sigma_E(\theta)$ being now determined, we insert Eq. (A3) into Eq. (A2) and integrate over all unwanted variables:

$$\begin{aligned} N(\theta, \varphi) &\propto \int\cdots\int N_{\rm exp}^{\rm inc}(E_d^{\rm inc}, i)\mathcal{W}(E)\sigma_E(\theta)A^{\rm MC}(v)\mathcal{T}(m, \varphi)d\{i\}dE_d^{\rm inc}dZ \\ &\equiv \langle\mathcal{T}\rangle_{\rm exp}^{E}(E_d^{\rm pol}, \theta, \varphi)N_0(\theta, \varphi) . \end{aligned} \tag{A5}$$

We recover here Eq. (17), together with the definition of the interpolated calibration data N_0,

$$N_0(\theta, \varphi) = \int\cdots\int N_{\rm exp}^{\rm inc}(E_d^{\rm inc}, i)\mathcal{W}(E)\sigma_E(\theta)A^{\rm MC}(v)d\{i\}dE_d^{\rm inc}dZ . \tag{A6}$$

For practical reasons, we used (interpolated) analyzing powers averaged over the vertex energies for the calibration data $\langle T_{kq}\rangle_{\rm cal}^{E}$ instead of $\langle T_{kq}\rangle_{\rm exp}^{E}$. The difference between these two terms is due to the deuteron incident energy spread for the Bates experiment and to slightly increasing analyzing powers below 80 MeV. In the case of T_{20}, this difference was evaluated to be much smaller than the systematic error on this quantity given in Table II.

[1] R. G. Arnold, B. T. Chertok, E. B. Dally, A. Grigorian, C. L. Jordan, W. P. Schütz, R. Zdarko, F. Martin, and B. A. Mecking, Phys. Rev. Lett. **35**, 776 (1975).
[2] P. E. Bosted *et al.*, Phys. Rev. C **42**, 38 (1990).
[3] M. E. Schulze *et al.*, Phys. Rev. Lett. **52**, 597 (1984).
[4] V. F. Dmitriev, D. M. Nikolenko, S. G. Popov, I. A. Rachek, Yu.M. Shatunov, D. K. Toporkov, E. P. Tsentalovich, Yu.G. Ukraintsev, B. B. Voitsekhovskii, and V.

G. Zelevinsky, Phys. Lett. **157B**, 143 (1985); B. B. Voitsekhovskii, D. M. Nikolenko, K. T. Ospanov, S. G. Popov, I. A. Rachek, D. K. Toporkov, E. P. Tsentalovich, and Yu.M. Shatunov, Pis'ma Zh. Eksp. Teor. Fiz. **43**, 567 (1986) [JETP Lett. **43**, 733 (1986)].
[5] R. Gilman *et al.*, Phys. Rev. Lett. **65**, 1733 (1990).
[6] B. Boden *et al.*, Z. Phys. C **49**, 175 (1991).
[7] G. E. Brown and A. D. Jackson, *The Nucleon-Nucleon Interaction* (North-Holland, Amsterdam, 1976).
[8] V. Z. Jankus, Phys. Rev. **102**, 1586 (1956).
[9] V. Glaser and B. Jakšić, Nuovo Cimento **5**, 1197 (1957).
[10] M. Gourdin, Nuovo Cimento **28**, 533 (1963); *Diffusion des Électrons de Haute Énergie* (Masson, Paris, 1966).
[11] E. L. Lomon, Ann. Phys. **125**, 309 (1980).
[12] D. Schildknecht, Phys. Lett. **10**, 254 (1964); Z. Phys. **185**, 382 (1965).
[13] R. G. Arnold, C. E. Carlson, and F. Gross, Phys. Rev. C **23**, 363 (1981).
[14] R. Prepost, R. M. Simonds, and B. H. Wiik, Phys. Rev. Lett. **21**, 1271 (1968).
[15] M. Garçon *et al.*, Nucl. Phys. **A458**, 287 (1986); E. J. Stephenson *et al.*, Indiana University Cyclotron Facility (IUCF) Scientific and Technical Report (1982), p. 163.
[16] J. M. Cameron *et al.*, Nucl. Instrum. Methods Phys. Res. **A305**, 257 (1991); note that in Eqs. (2) and (8), the T_{21} term should be multiplied by $\sin\varphi$ and not $\cos\varphi$; also in Eq. (9), the vector term should be multiplied by $2i$.
[17] I. The *et al.*, Phys. Rev. Lett. **67**, 173 (1991).
[18] I. The, Ph.D. thesis, Massachusetts Institute of Technology, 1992, unpublished.
[19] J. B. Flanz and C. P. Sargent, Nucl. Instrum. Methods **A241**, 325 (1985).
[20] P. C. Dunn, Nucl. Instrum. Methods **145**, 143 (1979).
[21] K. D. Williamson *et al.*, Adv. Cryo. Eng. **19**, 241 (1974).
[22] Bates Linear Accelerator Center Internal Report 88-1, 1988.
[23] W. Bertozzi, M. V. Hynes, C. P. Sargent, C. Creswell, P. C. Dunn, A. Hirsch, M. Leitch, B. Norum, F. N. Rad, and T. Sasanuma, Nucl. Instrum. Methods **141**, 457 (1977).
[24] S. Herron, B. S. thesis, Massachusetts Institute of Technology, 1981, unpublished.
[25] K. L. Brown, F. Rothacker, D. C. Carey, and Ch. Iselin, Report SLAC-91, Rev. 2, UC-28 (I/A), 1977.
[26] C. Kost and P. Reeve, TRIUMF Report TRI-DN-82-28, 1985; we acknowledge the help of G. M. Stinson for use of this code.
[27] LAMPF Internal Report MP-1-3401-3, 1986.
[28] D. R. Tieger *et al.*, Bates Technical Note 88-01, 1988.
[29] G. G. Ohlsen, Rep. Prog. Phys. **35**, 717 (1972); G. G. Ohlsen and P. W. Keaton, Jr., Nucl. Instrum. Methods **109**, 41 (1973).
[30] Particle Data Group, Phys. Rev. D **45**, P. 2, 1992, p. III.38.
[31] F. James and M. Roos, Comput. Phys. Commun. **10**, 343 (1975).
[32] M. Garçon, Nucl. Phys. **A508**, 445c (1990).
[33] S. Platckov, private communication.
[34] V. M. Muzafarov, V. E. Troitskiĭ, and S. V. Trubnikov, Fiz. Elem. Chastits. At. Yadra **14**, 1112 (1983) [Sov. J. Part. Nucl. **14**, 467 (1983)].
[35] S. Platchkov *et al.*, Nucl. Phys. **A510**, 740 (1990).
[36] J. A. Tjon, in *Hadronic Physics with Multi-GeV Electrons*, edited by B. Desplanques and D. Goutte (Nova Science, New York, 1991).
[37] M. Lacombe, B. Loiseau, J. M. Richard, R. Vinh Mau, J. Côté, P. Pirès, and R. de Tourreil, Phys. Rev. C **21**, 861 (1980).
[38] R. B. Wiringa, R. A. Smith, and T. L. Ainsworth, Phys. Rev. C **29**, 1207 (1984).
[39] R. Machleidt, K. Holinde, and Ch. Elster, Phys. Rep. **149**, 1 (1987).
[40] J. Pauschenwein, W. Plessas, and L. Mathelitsch, Few-Body Syst. Suppl. **6**, 195 (1992).
[41] B. Desplanques, Phys. Lett. B **203**, 200 (1988).
[42] M. I. Haftel, L. Mathelitsch, and H. F. K. Zingl, Phys. Rev. C **22**, 1285 (1980).
[43] V. M. Muzafarov and V. E. Troitskiĭ, Yad. Fiz. **33**, 1461 (1981) [Sov. J. Nucl. Phys. **33**, 783 (1981)].
[44] I. I. Belyantsev, V. K. Mitrjushkin, P. K. Rashidov, and S. V. Trubnikov, J. Phys. G **9**, 871 (1983).
[45] B. Mosconi and P. Ricci, Few-Body Syst. **6**, 63 (1989); **8**, 159(E) (1990).
[46] R. Schiavilla and D. O. Riska, Phys. Rev. C **43**, 437 (1991).
[47] B. Desplanques and A. Amghar, Z. Phys. A **344**, 191 (1992).
[48] M. P. Locher and A. Švarc, Z. Phys. A **338**, 89 (1991).
[49] F. Iachello, A. D. Jackson, and A. Lande, Phys. Lett. **43B**, 191 (1973).
[50] G. Höhler, E. Pietarinen, I. Sabba-Stefanescu, F. Borkowski, G. G. Simon, V. H. Walther, and R. D. Wendling, Nucl. Phys. **B114**, 505 (1976).
[51] S. Galster, H. Klein, J. Moritz, K. H. Schmidt, D. Wegener, and J. Bleckwenn, Nucl. Phys. **B32**, 221 (1971).
[52] M. Gari and W. Krümpelman, Z. Phys. A **322**, 689 (1986).
[53] A. Lung *et al.*, Phys. Rev. Lett. **70**, 718 (1993).
[54] M. Gari and H. Hyuga, Nucl. Phys. **A264**, 409 (1976).
[55] J. L. Friar, Ann. Phys. **81**, 332 (1973); F. Coester and A. Ostebee, Phys. Rev. C **11**, 1836 (1975); F. Gross and D. O. Riska, *ibid.* **34**, 1928 (1987).
[56] K. Tamura, T. Niwa, T. Sato, and H. Ohtsubo, Nucl. Phys. **A536**, 597 (1992).
[57] P. Sarriguren, J. Martorell, and D. W. L. Sprung, Phys. Lett. B **228**, 285 (1989).
[58] A. Amroun, V. Breton, J.-M. Cavedon, B. Frois, D. Goutte, J. Martino, X.-H. Phan, S. K. Platchkov, I. Sick, and S. Williamson, Phys. Rev. Lett. **69**, 253 (1992).
[59] R. Schiavilla, V. R. Pandharipande, and D. O. Riska, Phys. Rev. C **41**, 309 (1990); H. Henning, J. Adam, Jr., and P. U. Sauer, Few-Body Syst. Suppl. **5**, 133 (1992).
[60] R. Dymarz and F. C. Khanna, Nucl. Phys. **A507**, 560 (1990).
[61] P. G. Blunden, W. R. Greenberg, and E. L. Lomon, Phys. Rev. C **40**, 1541 (1989).
[62] P. Obersteiner, W. Plessas, and J. Pauschenwein, Few-Body Syst. Suppl. **5**, 140 (1992).
[63] P. A. M. Dirac, Rev. Mod. Phys. **21**, 392 (1949); F. Gross, in *Modern Topics in Electron Scattering*, edited by B. Frois and I. Sick (World Scientific, Singapore, 1991); J. Tjon, in [36].
[64] R. G. Arnold, C. E. Carlson, and F. Gross, Phys. Rev. C **21**, 1426 (1980).
[65] M. J. Zuilhof and J. A. Tjon, Phys. Rev. C **24**, 736 (1981); **22**, 2369 (1980).
[66] E. Hummel and J. A. Tjon, Phys. Rev. C **42**, 423 (1990).
[67] M. A. Braun and M. V. Tokarev, Fiz. Elem. Chastits At. Yadra **22**, 1237 (1991) [Sov. J. Part. Nucl. **22**, 601

(1991)].
[68] A. F. Krutov and V. E. Troitskiĭ, Yad. Fiz. **43**, 1327 (1986) [Sov. J. Nucl. Phys. **43**, 852 (1986)].
[69] R. S. Bhalerao and S. A. Gurvitz, Phys. Rev. Lett. **47**, 1815 (1981).
[70] G. Rupp and J. A. Tjon, Phys. Rev. C **41**, 472 (1990).
[71] N. Devine, Ph.D. thesis, University of Maryland, 1992, unpublished; private communication.
[72] P. L. Chung, F. Coester, B. D. Keister, and W. N. Polyzou, Phys. Rev. C **37**, 2000 (1988).
[73] L. L. Frankfurt, I. L. Grach, L. A. Kondratyuk, and M. I. Strikman, Phys. Rev. Lett. **62**, 387 (1989).
[74] A. P. Kobushkin and V. P. Shelest, Fiz. Elem. Chastits At. Yadra **14**, 1146 (1983) [Sov. J. Part. Nucl. **14**, 483 (1983)].
[75] V. V. Burov and V. N. Dostovalov, Z. Phys. A **326**, 245 (1987).
[76] T-S. Cheng and L. S. Kisslinger, Phys. Rev. C **35**, 1432 (1987).
[77] Y. Yamauchi and M. Wakamatsu, Nucl. Phys. **A457**, 621 (1986).
[78] H. Ito and A. Faessler, Nucl. Phys. **A470**, 626 (1987).
[79] H. Ito and L. S. Kisslinger, Phys. Rev. C **40**, 887 (1989).
[80] A. Buchman, Y. Yamauchi, and A. Faessler, Nucl. Phys. **A496**, 621 (1989).
[81] H. Dijk and B. L. G. Bakker, Nucl. Phys. **A494**, 438 (1989).
[82] T. H. R. Skyrme, Nucl. Phys. **31**, 556 (1962); E. Witten, *ibid.* **B223**, 422 (1983).
[83] E. M. Nyman and D. O. Riska, Nucl. Phys. **A468**, 473 (1987).
[84] M. Wakamatsu and W. Weise, Nucl. Phys. **A477**, 559 (1988).
[85] E. Braaten and L. Carson, Phys. Rev. D **39**, 838 (1989).
[86] S. J. Brodsky, Comments Nucl. Part. Phys. **12**, 213 (1984), and references therein.
[87] C. E. Carlson and F. Gross, Phys. Rev. Lett. **53**, 127 (1984).
[88] C. E. Carlson, Nucl. Phys. **A508**, 481c (1990).
[89] S. J. Brodsky and J. R. Hiller, Phys. Rev. D **46**, 2141 (1992).
[90] F. Coester, in *Proceedings of the International Conference on Medium and High-Energy Nuclear Physics*, Taipei, Taiwan, 1988, edited by W.-Y.P. Wang, K.-F. Liu, and Y. Tzeng (World Scientific, Singapore, 1989).
[91] J. S. Levinger, Acta Phys. Acad. Scient. Hung. **33**, 135 (1973).